IEEE Access
Multidisciplinary | Rapid Review | Open Access Journal

Received 11 November 2022, accepted 14 November 2022, date of publication 17 November 2022,
date of current version 29 November 2022.

Digital Object Identifier 10.1109/ACCESS.2022.3223118

RESEARCH ARTICLE

Implementing an Adaptive Thrust Distribution Algorithm on the Robust Control System for Serial Split-Hull Underwater Vehicles

VISHAKH S. KUMAR AND PRABHU RAJAGOPAL, (Member, IEEE)
Centre for Nondestructive Evaluation, Department of Mechanical Engineering, IIT Madras, Chennai 600036, India

Corresponding author: Vishakh S. Kumar (vishakhskumar1995@gmail.com)

This work was supported by the National Technology Centre for Ports, Waterways and Coasts, Indian Institute of Technology Madras, India.

ABSTRACT This paper discusses designing and implementing an adaptive thrust distribution algorithm on the already robust control system for serial split-hull underwater vehicles to maximise operational efficiency. Split-hull underwater vehicles are gaining popularity in subsea operations due to their flexible hyper-redundant design and enhanced manoeuvrability. These features facilitate them to replace conventional solutions, including torpedo-shaped Autonomous Underwater Vehicles (AUVs) and Remotely Operated Vehicles (ROVs). The field of research is currently undergoing a considerable transition toward operations on subsea activities that are more economical and efficient. Thus, implementing a robust and energy-efficient control system is of utmost importance. The robust Super Twisting Algorithm (STA) based control system is used on the vehicle, and an adaptive thrust distribution algorithm is proposed and implemented to optimise the energy efficiency further. The work involves modelling the vehicle, fluid forces, torque effects, and thruster configuration matrix and implementing the adaptive weight distribution on the STA-based control system. With the help of simulations, the improvements in the control system are proved.

INDEX TERMS Autonomous underwater vehicle, split-hull underwater vehicle, manoeuvrability, sliding mode control, adaptive thrust distribution.

I. INTRODUCTION

A. SERIAL SPLIT-HULL UNDERWATER VEHICLES

Underwater vehicles have gained popularity in the last few decades as they can be operated in deep and risky areas, which are challenging for human operators. Both Autonomous Underwater Vehicles (AUVs) [1], [2] and Remotely operated vehicles (ROVs) [3] are commonly used in the subsea environment for such operations. They are widely employed in the subsea oil and gas business and the scientific community [4]. They are appropriate for a variety of operations such as inspection, surveillance, maintenance, repair works and data mapping [5]. Serial split-hull underwater vehicles [6], [7] are a class of underwater vehicles with a design similar to Underwater Snake Robots (USR) [8], [9], but use rotary thrusters for locomotion instead of body undulating gait patterns [10]. Underwater Swimming Manipulator (USM) [11] is an example of such vehicles focusing on underwater intervention tasks and the CAD design of such a vehicle is shown in Fig. 1. They have excellent manoeuvrability compared to conventional torpedo-shaped AUVs and can operate in narrow and confined environments [12], [13]. Inspecting and maintaining subsea oil and gas installations is a widespread application of them [14]. The thrusters enable significantly improved agility compared to the undulating locomotion system used in USRs, also giving hovering capabilities [15]. The long slender hulls make them highly efficient and hydrodynamically similar to the normal AUVs, simultaneously giving the kinematic redundancy of the USRs. The ability to use the hulls as part of a manipulator to perform intervention tasks, as in the case of USMs, enables them to operate similar to ROVs [16]. Thus it can be said that a split-hull

The associate editor coordinating the review of this manuscript and approving it for publication was Mohammad Alshabi.

underwater vehicle is a hybrid combination of AUVs and ROVs.

The design of the control system for underwater vehicles, in general, is very complicated as it has to deal with uncertainties in the hydrodynamic parameters, unknown disturbances, and other unmodelled dynamic effects [17]. Due to the flexible design configurations of the split-hull vehicle, facilitated using the servo joints, additional forces during the relative motion between the hulls also have to be considered. In addition, they have lower body mass compared to typical ROVs and AUVs due to their slender design, making the joint motion significantly impact the overall motion of the vehicle [18]. These factors make controlling such vehicles more complex than other underwater vehicles. These challenges are explained in detail in [19] while designing a path following algorithm and in [20] and [21] while developing a basic control system incorporating the complex design of USMs. In addition, efficient utilisation of the resources [22] is crucial for operations such as water body mapping and intervention involving heading control and trajectory tracking over an extended period. There have been a few methods proposed to improve the energy efficiency of USMs, such as that given in [23]. With the help of rotary thrusters and rolling joints, the researchers proposed an efficient operation method for the vehicle. However, implementing such an improved mechanical system is very complicated, and it requires substantial modification to the existing structure of the vehicle. Thus, a method that can deliver efficient use of existing resources without significant modification to the vehicle is desirable in a practical view. The method proposed in [24] follows that approach by using a quadratic programming algorithm producing low errors and distributing the control signals almost uniformly among all thrusters, where the priority is given to reduce the wear and tear of the thrusters. However, the algorithm used needs considerable computational power and is unsuitable for budget-friendly vehicles. Considering all these aspects, this paper aims to achieve an efficient operation of the vehicle by introducing an improved thrust distribution algorithm with a priority given to low computational requirements. This algorithm is implemented on a robust control system proposed for USMs from the literature. More about the existing works on the control system on similar vehicles are explained next.

B. ROBUST CONTROL SYSTEM FOR THE UNDERWATER VEHICLES

There have been many attempts to develop a robust control system for underwater vehicles. A widely used non-linear control technique known as Sliding Mode Control (SMC) is particularly effective in situations when the system is subject to uncertainty, such as with underwater vehicles. In recent years, the SMC has been the subject of numerous findings for a variety of complicated dynamical systems. Some of its significant contributions made explicitly for the underwater vehicles are described in [25] and [26]. In [25], a set-point regulation of an underwater vehicle with

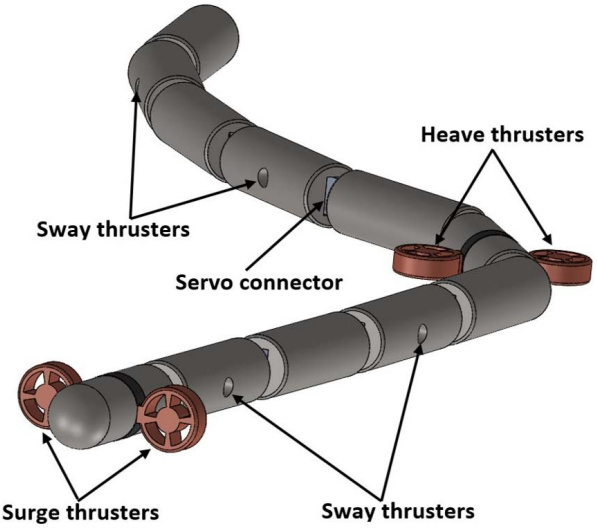

FIGURE 1. CAD design highlighting the servo joints and thrusters in an eleven-hull vehicle.

uncertainty in the hydrodynamic parameters is accomplished using a singularity-free SMC technique that was inspired by [27]. In [28], a hybrid control approach is created by combining the sliding mode with a virtual velocity algorithm for an Unmanned Underwater Vehicle (UUV) trajectory tracking control. Utilising SMC, the approach outlined in [29] manages multiplicative uncertainty in the thruster configuration matrix. A sliding mode with adaptive control is employed in [30], where the SMC is employed with adaptive PID-based controller gains and a real-time update on the upper bound on the disturbances. SMC can also be utilised to control coupling effects between an attached manipulator arm and the underwater vehicle, as stated in [31] and linearisation errors, as given by [32]. The combined use of backstepping and SMC is investigated for an underwater vehicle in [33]. A sliding mode-based adaptive control is used for the attitude control of underwater vehicles in [34], and a fuzzy sliding mode is implemented for the formation control of underactuated AUVs in [35]. An observer-based backstepping finite time SMC technique is proposed by [26] for the trajectory tracking of underwater vehicles subject to unknown system uncertainties and time-varying external disturbances. To accomplish robust tracking of a desired gait pattern and underactuated straight-line path following, sliding mode techniques are applied to land-based snake robots in [36]. The model presented in [37] is very close to the one used in this paper but uses a PD controller for tracking the position and heading along the reference path instead.

In the first-order relay controller, which is closely related to the SMC, significant chattering issues exist [30]. A saturated control [38] can be employed to eliminate this undesirable behaviour; however, when parasitic dynamics are taken into account, the efficiency of the controller is challenged because sliding mode does not exist [39] in the boundary layer. As a result, the Super Twisting Algorithm (STA) is employed, one of the most efficient second-order continuous

SMC algorithms. It reduces chattering issues and provides a smoother control signal, and it has been used in various applications since its introduction [40]. A conservative upper bound must be employed when designing the controller to ensure that sliding is maintained because the STA works only with bounded disturbances. This restriction can be overcome with adaptive STA [41], where the gains can be changed to keep the sliding constant while keeping the value as minimal as possible. The position and speed of the vehicle must be known because the STA can be applied to the systems only if the control input is present in the first derivative of the sliding variable [42], [43]. When they are not available, the states are determined using a higher-order Sliding Mode Observer (SMO), as recommended in [44]. The work in [45] presents an improved model to swap the PD controller with an STA and a higher-order SMO in the scenario where only the position measurements are available. The results from [41], [44], and [46] are combined in [11] where they improved the normal STA using a system with adaptive gains.

A similar approach is followed in this paper, but an adaptive thrust distribution algorithm is implemented as an extension to optimise the overall power consumption. After implementing the control and state observer systems to the vehicle and demonstrating the ultimate boundedness of the tracking errors, more specifics regarding this algorithm will be covered in section V. Simulations are performed to verify the theoretical findings and show that the proposed approach is suitable for controlling split-hull underwater vehicles. The findings are compared with those of existing solutions to determine how well the proposed solution performs in relation to the current ones.

To the best of the authors' knowledge, no prior research has considered the thorough analysis and comparison of the different thrust distribution modes of a split-hull underwater vehicle using rotary thrusters. Analysis and optimisation of the thrust distribution of such vehicles, which have received little prior research, significantly contribute as they gain more and more research attention. The main idea and conclusions of this work will therefore be helpful during the development of similar vehicles, and further details of this research are provided next.

C. VALIDITY OF THE OUTCOMES OF THE PAPER

This paper uses simulation results to prove the proposed adaptive thrust distribution algorithm and does not go with experimental validation for the same. The primary reason is that it is an extension of the work in [11] by focussing on optimising the control signals to reduce overall thrust requirement during the operation. All subparts of this work are proved with experiments in the related studies [11], [47]. For instance, the vehicle model is validated through experiments in [8] and [48]. In addition, the authors have verified the modelling accuracy of the split-hull underwater vehicles as given in [6], [7]. Also, the control system and the state estimator (SMO), discussed in section III, are validated in the actual scenario in [47] and [49]. In short, experimental validation is not necessary to prove the outcomes of the paper. Hence, the analysis is continued with simulation results.

D. ORGANISATION OF THE PAPER

This paper is organised as follows. Vehicle model synthesis is carried out first in section II, followed by the design of the sliding mode controller and observer systems in section III, which are analysed for stability in section IV. The simulation methodology is explained in section V, introducing the concept of the adaptive thrust distribution. Various thrust distributions are considered and compared to choose the optimum one in section VI. It is continued with conclusions in section VII and suggestions for future research in section VIII.

II. VEHICLE MODEL SYNTHESIS

Note that this paper considers general elliptical/cylindrical hulls as it is the most commonly used in the industry [50]. However, the proposed concepts can be applied to any split-hull underwater vehicle as long as it can be mathematically modelled and has multiple thrusters making it over-actuated. More about this will be discussed in section VII. The model synthesis starts with the vehicle kinematic modelling that serves as the basis for the whole analysis. Then the fluid force and torque acting on the vehicle will be computed in the dynamic modelling. Table 1 explains the key parameters used for the analysis. The design of the split-hull vehicle is the same as the one shown in Fig. 1, which includes eleven cylindrical hulls connected serially using servo joints. The surge thrusters are attached to the front hull, whereas the heave thrusters are attached to the middle hull. Four internal sway thrusters are fixed at specific locations as per Table 2. More details about the vehicle and the proposed configurations are discussed in section V, and additional details are given in [6].

A. KINEMATIC MODELLING

A few important points about the kinematic modelling are as follows. The hulls are considered as links for the multi-body analysis. The vehicle is designed to move in the horizontal (XY) plane, fully submerged in water, and has $N+2$ degrees of freedom that includes N hull orientation angles and the XY position of the vehicle Centre of Mass (C.M). The orientation of each hull is denoted by $\theta_i,\ i \in [1, 2 \ldots, N]$ and is defined as the angle that the hull forms with the global X axis in the positive anticlockwise direction. The basic kinematic parameters of a general N hull vehicle are shown in Fig. 2, and all necessary parameters used for the multi-body analysis are given in (4) - (27). The joint angles are represented by ϕ_{ij} and are given as

$$\phi_{ij} = \theta_j - \theta_i,\ \ j = i+1,\ i \in [1, 2, \ldots, N-2] \qquad (1)$$

The heading of the vehicle is given by the orientation of the leading hull (θ_N), and more about this will be described in section V-B. The local coordinate system (xy) of each hull is fixed in the C.M of the hull with x in the axial and y in the

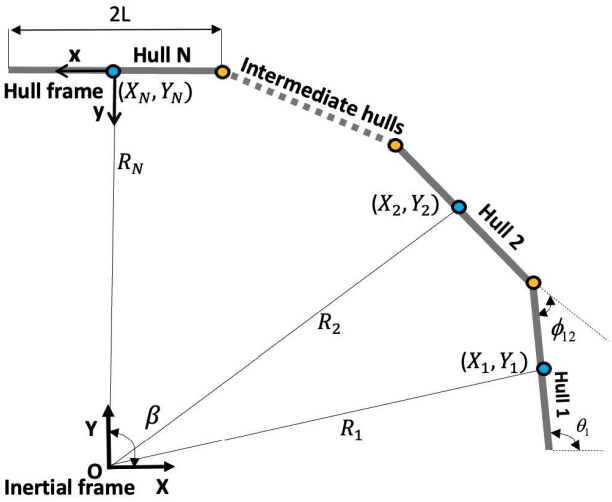

FIGURE 2. Schematic depiction of the kinematic parameters of an N hull vehicle.

lateral/normal directions. The rotation matrix from the i^{th} hull coordinates to the global one is given by

$$T_i = \begin{bmatrix} \cos(\theta_i) & -\sin(\theta_i) \\ \sin(\theta_i) & \cos(\theta_i) \end{bmatrix} \in \mathbb{R}^{2\times 2}. \tag{2}$$

The coordinates of the C.M of the vehicle are given by

$$P_{\text{CM}} = \begin{bmatrix} P_X \\ P_Y \end{bmatrix} = \begin{bmatrix} \frac{1}{m_{tot}} \sum_1^N m_i X_i \\ \frac{1}{m_{tot}} \sum_1^N m_i Y_i \end{bmatrix} = \frac{1}{m_{tot}} \begin{bmatrix} e^{\text{T}} MX \\ e^{\text{T}} MY \end{bmatrix}. \tag{3}$$

where (X_i, Y_i) are the global coordinates of the C.M of i^{th} hull. In addition, M is the mass matrix given in (7), and X and Y are the global position coordinate vectors as given in (10).

$$D_o = \begin{bmatrix} 1 & -1 & 0 & 0 & 0 & 0 & \dots & 0 \\ 0 & 1 & -1 & 0 & 0 & 0 & \dots & 0 \\ . & . & . & . & . & . & . & . \\ . & . & . & . & . & . & . & . \\ 0 & 0 & 0 & 0 & . & . & 1 & -1 \end{bmatrix} \in \mathbb{R}^{(N-1)\times N} \tag{4}$$

$$A_o = \begin{bmatrix} 1 & 1 & 0 & 0 & 0 & 0 & \dots & 0 \\ 0 & 1 & 1 & 0 & 0 & 0 & \dots & 0 \\ . & . & . & . & . & . & . & . \\ . & . & . & . & . & . & . & . \\ 0 & 0 & 0 & 0 & . & . & 1 & 1 \end{bmatrix} \in \mathbb{R}^{(N-1)\times N} \tag{5}$$

$$e = [1\ 1\ 1\ .\ .\ 1]^{\text{T}}, \quad \theta = [\theta_1\ \theta_2\ \dots \theta_N]^{\text{T}} \in \mathbb{R}^{N\times 1} \tag{6}$$

$$M = diag\left(\begin{bmatrix} m_1 & m_2 & \dots & m_N \end{bmatrix}\right) \in \mathbb{R}^{N\times N} \tag{7}$$

$$L = diag([L_1\ \dots\ L_N]),\ J = diag([J_1\ \dots\ J_N]) \in \mathbb{R}^{N\times N} \tag{8}$$

$$V_f = diag([V_{f1}\ V_{f2}\ \dots\ V_{fN}]) \in \mathbb{R}^{N\times N} \tag{9}$$

$$X = [X_1\ X_2\ \dots X_N]^{\text{T}}, \quad Y = [Y_1\ Y_2\ \dots Y_N]^{\text{T}} \in \mathbb{R}^{N\times 1} \tag{10}$$

$$\sin(\theta) = [\sin(\theta_1)\ \ \sin(\theta_2)\ \ \dots\ \ \sin(\theta_N)]^{\text{T}} \in \mathbb{R}^{N\times 1} \tag{11}$$

$$\cos(\theta) = [\cos(\theta_1)\ \ \cos(\theta_2)\ \ \dots\ \ \cos(\theta_N)]^{\text{T}} \in \mathbb{R}^{N\times 1} \tag{12}$$

$$S_\theta = diag([\sin(\theta_1)\ \ \sin(\theta_2)\ \ \dots\ \ \sin(\theta_N)]) \in \mathbb{R}^{N\times N} \tag{13}$$

$$C_\theta = diag([\cos(\theta_1)\ \ \cos(\theta_2)\ \ \dots\ \ \cos(\theta_N)]) \in \mathbb{R}^{N\times N} \tag{14}$$

$$C_t = diag([C_{t1}\ \dots\ C_{tN}]),\ C_n = diag([C_{n1}\ \dots\ C_{nN}]) \in \mathbb{R}^{N\times N} \tag{15}$$

$$\mu_n = diag([\mu_{n1}\ \mu_{n2}\ ..\ \mu_{nN}]) \in \mathbb{R}^{N\times N} \tag{16}$$

$$T = \begin{bmatrix} C_\theta & -S_\theta \\ S_\theta & C_\theta \end{bmatrix} \in \mathbb{R}^{2N\times 2N} \tag{17}$$

$$V = LA_o^{\text{T}}(D_o M^{-1} D_o^{\text{T}})^{-1} A_o L \in \mathbb{R}^{N\times N} \tag{18}$$

$$K = LA_o^{\text{T}}(D_o M^{-1} D_o^{\text{T}})^{-1} D_o M^{-1} \in \mathbb{R}^{N\times N} \tag{19}$$

$$K_1 = S_\theta K S_\theta + C_\theta K C_\theta, \quad K_2 = S_\theta K C_\theta - C_\theta K S_\theta \tag{20}$$

$$V_1 = S_\theta V S_\theta + C_\theta V C_\theta, \quad V_2 = S_\theta V C_\theta - C_\theta V S_\theta \tag{21}$$

$$\Lambda_1 = diag([\lambda_{1,1}\ \lambda_{1,2} \dots\ \lambda_{1,N}]) \in \mathbb{R}^{N\times N} \tag{22}$$

$$\Lambda_2 = diag([\lambda_{2,1}\ \lambda_{2,2}\ \dots\ \lambda_{2,N}]) \in \mathbb{R}^{N\times N} \tag{23}$$

$$\Lambda_3 = diag([\lambda_{3,1}\ \lambda_{3,2} \dots\ \lambda_{3,N}]) \in \mathbb{R}^{N\times N} \tag{24}$$

$$M_\theta = J + V_1 + K_1 \mu_n K_1^{\text{T}} + \Lambda_1 \in \mathbb{R}^{N\times N} \tag{25}$$

$$W_\theta = V_2 - K_1 \mu_n K_2^{\text{T}} \in \mathbb{R}^{N\times N} \tag{26}$$

$$V_\theta = \Lambda_2 - K_1 \mu_n (C_\theta V_{fX} + S_\theta V_{fY}) \in \mathbb{R}^{N\times N} \tag{27}$$

The overall hull constraint equations are given as

$$D_o X + LA_o \cos(\theta) = 0 \quad D_o Y + LA_o \sin(\theta) = 0. \tag{28}$$

Rearranging this gives the position characteristic equations of the split-hull vehicle as follows.

$$X = -K^{\text{T}} \cos(\theta) + eP_X \ \ Y = -K^{\text{T}} \sin(\theta) + eP_Y \tag{29}$$

where the matrix K is given by (19). Differentiating (29) gives the velocity characteristic vector as follows.

$$\dot{X} = K^{\text{T}} S_\theta \dot{\theta} + e\dot{P}_X \ \ \dot{Y} = -K^{\text{T}} C_\theta \dot{\theta} + e\dot{P}_Y \tag{30}$$

Further differentiation gives the acceleration characteristics as shown below.

$$\ddot{X} = K^{\text{T}}(C_\theta \dot{\theta}^2 + S_\theta \ddot{\theta}) + e\ddot{P}_X \ \ \ddot{Y} = K^{\text{T}}(S_\theta \dot{\theta}^2 - C_\theta \ddot{\theta}) + e\ddot{P}_Y \tag{31}$$

B. DYNAMIC MODELLING

The model should take into account all the fluid forces that are crucial for the control system design. Drag force (F_D) and added mass force (F_A) are the main external fluid forces that come into action. Each hull is a slender cylinder [51] with a length greater than 2.7 times the diameter, so the slender body theory [52] and hence the Morison's equation [53] can be applied to calculate the fluid forces. The net Z direction force on each hull is zero due to the neutrally buoyant design, as the forces of buoyancy and gravity nullify. However, the Coriolis and centrifugal forces must be considered, and they are used for estimating the force acting on the hulls. After

TABLE 1. List of parameters used for the dynamic analysis.

Symbol	Meaning
θ_i	i^{th} hull orientation with X axis (rad)
ϕ_{ij}	ij^{th} joint angle (rad)
m_i	i^{th} hull mass (kg)
$2L$	Hull length (m)
$2a, 2b$	Hull major and minor axis lengths (m)
r	Hull radius $(D/2) = 0.05$ m
R	Radius of the curvature of the path (m)
ρ	Fluid density (1000 kg/m^3)
v_r	Relative vehicle velocity in hull coordinates (m/s)
C_{ti}	i^{th} hull axial drag coefficient (kg/m)
C_{ni}	i^{th} hull lateral drag coefficient (kg/m)
μ_{ni}	i^{th} hull lateral added mass coefficient (kg)
$h_{(i,j)}$	ij^{th} joint constraint force (N)
f_{fi}	i^{th} hull fluid force in hull coordinates (N)
τ_{fi}	i^{th} hull fluid torque (Nm)
$\tau_{(i,j)}$	ij^{th} joint torque (Nm)
f_{ti}	i^{th} hull thrust (N)

using the kinematic modelling, which gives the instantaneous velocity and acceleration values, (39) is used to calculate the hydrodynamic forces. The individual hull forces are calculated first, and to evaluate the net fluid force acting on the vehicle, they are combined in the global coordinates as given in (44). Each step is explained separately as follows.

1) MODELLING THE BASIC ASPECTS OF THE VEHICLE

A generic hull with an elliptical cross-section is considered with corresponding semi-major axis (a) and semi-minor axis (b) lengths. The cylindrical hull employed in this paper is a specific case of the elliptical hull with $a = b = r$. To take into consideration the effect of thrusters, the parameters must be changed, as in the case of the front and middle hulls. The thruster's outer diameter is $d_{to} = 0.1$ m, and its height is $h_t = 0.056$ m. Equation (32) provides the parameters for the front hull, which is equipped with surge thrusters.

$$a = (2r + d_{to}(h_t/2L))/2, \quad b = r. \tag{32}$$

The parameters for the middle hull, where the heave thrusters are mounted, are given by

$$a = (2r + d_{to}(d_{to}/2L))/2, \quad b = r. \tag{33}$$

Keep in mind that for the remaining hulls, $a = b = r$. While choosing the length of hulls to consider the impact of thrusters, L_e is used as the effective length. It is equal to $2L+2h_t$ for the front hull, $2L+2d_t/3$ for the middle hull and $2L$ for the remaining hulls. When it comes to the mass, each hull's total mass must satisfy the neutral buoyancy criterion. The masses of all hulls, except for the N^{th} and centre hulls, are given by

$$m_i = \frac{\pi}{4}D^2(2L)\rho, \quad i \in [1, N-1],\ i \neq (N+1)/2. \tag{34}$$

The total masses of the N^{th} and middle hulls are different due to the presence of external thrusters and their supports as given by (35), where m_{tb} is the net buoyancy on the thruster.

$$m_N = m_{(N+1)/2} = \frac{\pi}{4}D^2(2L)\rho + 2m_{tb} \tag{35}$$

Moment of inertia (J) about the z-axis for each hull with mass m and length $2L$ is given by (36). It will be slightly different for the leading and middle hulls due to the thrusters, as in the case of the mass. To do that, each thruster is considered as a hollow cylinder of mass m_t with outer radius $r_{to} = d_{to}/2 = 0.05$ m and inner radius $r_{ti} = 0.038$ m. The offset of each thruster from the axis of the hull is $l_{\text{off}} = 0.11$ m. The parallel axis theorem gives the following moment of inertia values. For all the hulls with no thrusters attached, only the contribution of the hull will be used. Hence,

$$J_i = m_i\frac{(2L)^2}{12} \quad i \in [1, N-1],\ i \neq (N+1)/2. \tag{36}$$

For the middle hull, it is given by

$$J_{(N+1)/2} = (m_{(N+1)/2} - 2m_t)\frac{(2L)^2}{12} + m_t(r_{to}^2 + r_{ti}^2 + 2l_{\text{off}}^2). \tag{37}$$

For the leading hull, it is given by

$$J_N = (m_N - 2m_t)\frac{(2L)^2}{12} + \frac{m_t}{6}(3(r_{to}^2 + r_{ti}^2) + h_t^2 + 12l_{\text{off}}^2). \tag{38}$$

2) MODELLING THE FLUID FORCES

The modelling of the forces acting on the individual hulls and the calculation of the net fluid force on the vehicle are both covered in this section. The total external fluid force acting on the i^{th} hull is determined in global coordinates as the sum of the added mass force (F_{Ai}) and drag force (F_{Di}).

$$F_{fi} = F_{Ai} + F_{Di} \tag{39}$$

By converting the hull coordinates (f_{Ai}) into global/inertial coordinates according to (40), where C_A is the added mass coefficient matrix, the added mass force for the i^{th} hull (F_{Ai}) is obtained. As shown below, $\dot{v}_{ri}$ is the hull's relative acceleration matrix defined along the hull coordinates.

$$F_{Ai} = T_i f_{Ai} = -T_i C_{Ai}\dot{v}_{ri} \tag{40}$$

$$\dot{v}_{ri} = \begin{bmatrix}\dot{v}_{rxi} & \dot{v}_{ryi}\end{bmatrix}^{\mathrm{T}},\ C_{Ai} = \begin{bmatrix}0 & 0\\ 0 & \mu_{ni}\end{bmatrix} = \begin{bmatrix}0 & 0\\ 0 & \rho\pi C_a a^2 L_e\end{bmatrix} \tag{41}$$

The lateral drag coefficient denoted C_a will be discussed after this section and depends on the flow, body size, and shape. Because it is significantly less in proportion to the total mass for a slender body, the added mass force in the x direction is negligible [54]. The drag force (F_{Di}) is provided below and is taken to be a function of the first and second orders of the relative hull velocity (v_{ri}) defined in the hull frame.

$$F_{Di} = T_i f_{Di} = -T_i(C_{Di}v_{ri} + C_{Di}v_{ri}|v_{ri}|) \tag{42}$$

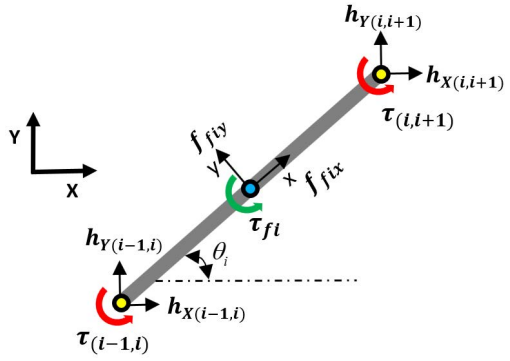

FIGURE 3. Schematic diagram of the fluid forces and torques acting on the i^{th} hull.

C_{Di} is the drag coefficient matrix for the i^{th} hull, which is given by

$$C_{Di} = \begin{bmatrix} C_{ti} & 0 \\ 0 & C_{ni} \end{bmatrix} = \begin{bmatrix} \frac{1}{2}\rho\pi C_f \frac{(a+b)}{2} L_e & 0 \\ 0 & \frac{1}{2}\rho C_d (2a) L_e \end{bmatrix}. \quad (43)$$

The components of the total external force on the i^{th} hull denoted by f_{fi} are illustrated in Fig. 3. It is calculated by adding the corresponding terms for additional mass and drag force ($f_{Ai}+f_{Di}$). Internal forces between the hulls, represented in the same figure as (h_X, h_Y), are not required for the analysis and are not addressed in detail in this paper. Being internal forces, they appear only in the force balance of individual hulls as given in (61) and (62). V_f given in (9) is the fluid velocity vector expressed in the inertial coordinates. It can be defined along both X and Y directions as used in (27). Given that stagnant water is taken into account, all terms in V_f are zero, and as a result, the relative velocity is the same as the actual vehicle velocity. Drag coefficients are expressed as C_f for the x-direction and C_d for the y-direction, respectively. The relative velocity matrix in i^{th} hull frame is given by $v_{ri} = \begin{bmatrix} v_{rxi} & v_{ryi} \end{bmatrix}^{\mathrm{T}}$. The multi-body external force matrix is created by merging the individual hull external force matrices, as shown below.

$$F_f = F_D + F_A \in \mathbb{R}^{2N\times 1} \quad (44)$$

$F_D \in \mathbb{R}^{2N\times 1}$ is the total drag matrix and $F_A \in \mathbb{R}^{2N\times 1}$ is the total added mass force matrix. The X component forces make up the first N terms in each matrix, while the Y component forces, which correspond to each hull, make up the remaining terms. The external force matrix given in (44) can be calculated separately for each hull using the formulas in (40) and (42), but it becomes more difficult as the number of hulls increases. As a result, the calculation is made simpler by using the multi-body matrices provided in (4) - (27).

$$F_D = -\begin{bmatrix} C_t C_\theta & -C_n S_\theta \\ C_t S_\theta & C_n C_\theta \end{bmatrix} \left(\begin{bmatrix} v_{rx} \\ v_{ry} \end{bmatrix} + \begin{bmatrix} sgn(v_{rx}) v_{rx}^2 \\ sgn(v_{ry}) v_{ry}^2 \end{bmatrix} \right) \quad (45)$$

$$F_A = -\begin{bmatrix} \mu_n S_\theta^2 & -\mu_n S_\theta C_\theta \\ -\mu_n S_\theta C_\theta & \mu_n C_\theta^2 \end{bmatrix} \begin{bmatrix} \ddot{X} \\ \ddot{Y} \end{bmatrix} \quad (46)$$

The terms v_{rx} and $v_{ry} \in \mathbb{R}^{N\times 1}$ can be found by converting the global velocity values from (30) to the surge and sway velocity matrices given in hull coordinates as

$$\begin{bmatrix} v_{rx} \\ v_{ry} \end{bmatrix} = T^{\mathrm{T}} \begin{bmatrix} \dot{X} \\ \dot{Y} \end{bmatrix} \in \mathbb{R}^{2N\times 1}. \quad (47)$$

3) MODELLING THE JOINT TORQUE REQUIREMENT

For the analysis of vehicle motion, estimating the joint torque requirement is essential. This torque is necessary to balance out two components: one caused by the centrifugal force ($m_i R\omega^2$) on each hull and the other by the external normal fluid force (τ_{fi}) on the hull, which is discussed below. Keep in mind that joint torque is crucial for the split-hull vehicle because it determines whether the joints can control specific hull angles. Here, the technique employed in [8], where the model of an underwater snake robot having elliptical cross-section hulls was experimentally validated, is used. For the i^{th} hull, the fluid torque acting is given by

$$\tau_{fi} = -(\lambda_1 \ddot{\theta}_i + \lambda_2 \dot{\theta}_i + \lambda_3 \dot{\theta}_i |\dot{\theta}_i|). \quad (48)$$

The first term represents the fluid torque generated by the added mass effect on the hull ($-\lambda_1 \ddot{\theta}_i$), and the fluid torque caused by the drag pressure between the opposing sides of the hull in the lateral (y) direction is expressed by the remaining terms with the coefficients λ_2 and λ_3. It should be noted that both linear and quadratic drag forces are taken into account. The parameters λ_1, λ_2 and λ_3 are determined for the general elliptical hull [8] and are shown below. These parameters depend on the size and shape of the hull.

$$\lambda_1 = \frac{1}{12}\rho\pi C_M (a^2 - b^2)^2 L^3, \quad \lambda_2 = \frac{1}{6}\rho\pi C_f (a+b) L^3,$$
$$\lambda_3 = \frac{1}{8}\rho\pi C_f (a+b) L^4 \quad (49)$$

The added mass term will be zero for cylindrical hulls (as $a = b = r$), but it is a non-zero value for the front and centre hulls because of the presence of thrusters. Note that C_M is the added mass torque coefficient. The i^{th} hull's torque balance is written as

$$J\ddot{\theta}_i = \tau_{(i)(i+1)} - \tau_{(i-1)(i)} + \tau_{fi} - L(\sin(\theta_i)(h_{X(i,i+1)} - h_{X(i-1,i)}) - \cos(\theta_i)(h_{Y(i,i+1)} - h_{Y(i-1,i)})). \quad (50)$$

It consists of all the internal forces ($h_{i,i+1}$), the fluid torque (τ_{fi}) and the joint torques ($\tau_{(i)(j)}$). The updated fluid coefficients are estimated next.

4) ESTIMATION OF THE UPDATED FLUID COEFFICIENTS

The hydrodynamic coefficients must be carefully chosen to ensure the accuracy of the results. With a maximum speed of 0.5 m/s and a Reynolds number of about 10^5, the steady-state flow in the transition region described by [55] is employed in this case. Numerous investigations have been conducted on the force acting on slender bodies under identical circumstances. A few of these are discussed in [8] and [56]

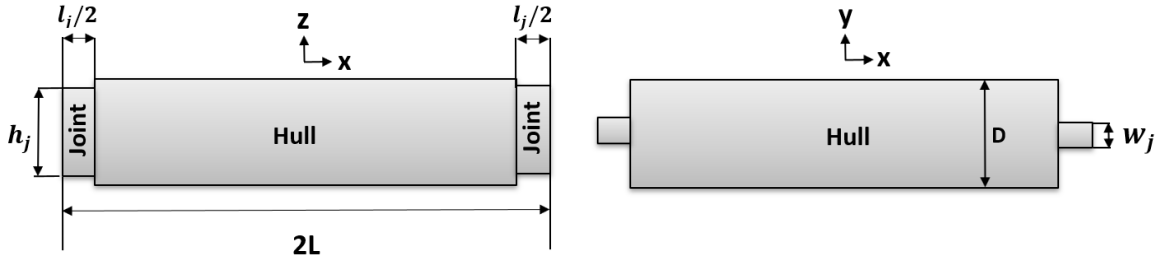

(a) Side view (b) Top view

FIGURE 4. Schematic diagrams showing the dimensions of an inner hull with servo joints.

and utilise the added mass coefficients $C_{M0} = C_{a0} = 1$ and the drag coefficients $C_{d0} = 1$, $C_{f0} = 0.03$. However, they took into account smooth, uniform cylinders, which is not the case here due to the discontinuity introduction by the servo joints. The CAD design of the hull is shown in Fig. 4 with the important dimensions indicated. By computing the updated fluid coefficients that take into account the effect of servo joints as given by the authors [6], this issue can be resolved. To do this, the discontinuity factor (d_{fx}), a new parameter that is defined as the ratio of the net servo joint length ($l_j = 0.065$ m) to the effective length of the hull (L_e), is introduced as follows.

$$d_{fx} = \frac{l_j}{L_e}, \quad d_{fz} = \frac{h_j}{L_e}, \quad S_h = \frac{L_e}{D}. \tag{51}$$

Using another parameter designated as d_{fz}, the height of the joint is related to the length of the hull. The servo joint is viewed as a thin rectangular block attached to the hull because of its low width ($w_j = 0.027$ m) in relation to its height ($h_j = 0.08$ m) as well as the effective length of the hull. It should be noticed that the joint section (l_j, h_j) has identical dimensions for all hull configurations. The effective slenderness of the hull (S_h) is introduced in addition to these characteristics. It is defined as the ratio of the effective length (L_e) and the effective diameter ($2R$) of the hull. Since only one servo joint is connected to both 1^{st} and N^{th} (outer) hulls, the corresponding d_{fx} values are lower in comparison to the inner hulls. Based on this, the updated fluid coefficients are obtained and validated by the authors [6] as

$$C_f = C_{f0}(1 + 4.01 d_{fx}), \quad C_d = C_{d0}(1 + 1.4 d_{fx}). \tag{52}$$

These equations will be applied to all the hulls, and before starting the simulation, the thrust forces have to be incorporated in the multi-body matrix form.

5) MODELLING THE THRUST FORCE ALLOCATION

The overall effect of the thrusters on the vehicle C.M is given by

$$\tau_{\text{CM}} = \begin{bmatrix} F_{\text{CM},X} \\ F_{\text{CM},Y} \\ M_{\text{CM},Z} \end{bmatrix} = \begin{bmatrix} e^{\text{T}} & 0^{1\times N} \\ 0^{1\times N} & e^{\text{T}} \\ e^{\text{T}} S_\theta K & -e^{\text{T}} C_\theta K \end{bmatrix} \begin{bmatrix} F_{tX} \\ F_{tY} \end{bmatrix} = T_c f_t \tag{53}$$

where T_c is the thruster configuration matrix which is a function of the hull angles (θ_i) and $f_t = [f_{t,k_1}, f_{t,k_2}, \ldots f_{t,k_r}]^{\text{T}}$ is the vector of thrust forces. T_c is the mapping between the thruster forces and the net force and moment acting on the C.M of the vehicle. It is given by (54), where B_X, B_Y are the functions of the instantaneous angular orientations of the thrusters and are obtained by extending b_X and b_Y as given in [37]. The steps involve making the 2-dimensional vector by filling the b_i values where thrusters are present and by zero where thrusters are absent.

$$T_c(\theta) = \begin{bmatrix} b_X^{\text{T}} \\ b_Y^{\text{T}} \\ e^{\text{T}}(S_\theta K B_X^{\text{T}} - C_\theta K B_Y^{\text{T}}) \end{bmatrix} \tag{54}$$

$$\begin{bmatrix} F_{tX} \\ F_{tY} \end{bmatrix} = \begin{bmatrix} B_X^{\text{T}} \\ B_Y^{\text{T}} \end{bmatrix} f_t \quad B_X(b_X), B_Y(b_Y) \in \mathbb{R}^{r\times N} \tag{55}$$

$$b_X = [\cos(\theta_{k_1} + \alpha_{k_1}) \ \ldots \ \cos(\theta_{k_r} + \alpha_{k_r})]^{\text{T}} \in \mathbb{R}^{r\times 1} \tag{56}$$

$$b_Y = [\sin(\theta_{k_1} + \alpha_{k_1}) \ \ldots \ \sin(\theta_{k_r} + \alpha_{k_r})]^{\text{T}} \in \mathbb{R}^{r\times 1} \tag{57}$$

Note that θ_{k_i} is the orientation of the hull where the thruster is fixed, and α_{k_i} is the relative orientation of the thruster with respect to the hull. The thrust forces act through the C.M of the corresponding hull. The major objective of the force allocation problem is to distribute the total work between multiple thrusters to produce the desired forces and moments.

$$\tau_{\text{CM},des} = \begin{bmatrix} F_{\text{CM},des} \\ M_{\text{CM},des} \end{bmatrix} = \begin{bmatrix} F_{\text{CM},des_X} \\ F_{\text{CM},des_Y} \\ M_{\text{CM},des} \end{bmatrix} = T_c(\theta) f_t \tag{58}$$

As the vehicle has more thrusters than the number of coordinates to be controlled, the vehicle is over-actuated, which means secondary objectives can be added to the force allocation problem. Hence, an objective is given to minimise the effort of the thrusters, which minimises the power consumption. With minimum thruster effort as the optimisation criteria, a least-square optimisation problem is proposed as follows.

$$\text{Minimise } f_t^{\text{T}} W f_t \quad \text{where} \quad \tau_{\text{CM},des} - T_c f_t = 0 \tag{59}$$

The explicit solution to this optimisation problem is given in [57] as

$$f_t = T_c^* \tau_{\mathrm{CM},des} \in \mathbb{R}^{r\times 1}, \quad T_c^* = W^{-1}T_c^{\mathrm{T}}(T_c W^{-1} T_c^{\mathrm{T}})^{-1}. \tag{60}$$

T_c^* is the generalised inverse allocator, and W is the matrix specifying the relative weighting between the thrusters. The weight values are analysed in detail for the optimisation problem, which will be discussed in section V-C. The overall dynamics of the vehicle has to be obtained as it is essential for implementing the control system.

C. OVERALL DYNAMICS OF THE VEHICLE

Before going into the overall dynamics of the vehicle, the force balance equations of the i^{th} hull are given by

$$m_i \ddot{X}_i = h_{X(i,i+1)} + h_{X(i-1,i)} + F_{fiX} + F_{tiX} \tag{61}$$
$$m_i \ddot{Y}_i = h_{Y(i,i+1)} + h_{Y(i-1,i)} + F_{fiY} + F_{tiY}. \tag{62}$$

Note that h is an internal force, and hence it will get cancelled out in the overall dynamics of the vehicle, which can be expressed in the global coordinates as

$$m_{tot}\ddot{P}_X = e^{\mathrm{T}}(F_{fX} + F_{tX}) \quad m_{tot}\ddot{P}_Y = e^{\mathrm{T}}(F_{fY} + F_{tY}). \tag{63}$$

Inserting (31) and (44) in (63) yields the final equations for the acceleration of the C.M.

$$\begin{bmatrix}\ddot{P}_X \\ \ddot{P}_Y\end{bmatrix} = M_P^{-1}\Bigg(\begin{bmatrix}e^{\mathrm{T}}F_{DX} + F_{\mathrm{CM},X} \\ e^{\mathrm{T}}F_{DY} + F_{\mathrm{CM},Y}\end{bmatrix} - \begin{bmatrix}e^{\mathrm{T}}\mu_n S_\theta^2 & -e^{\mathrm{T}}\mu_n S_\theta C_\theta \\ -e^{\mathrm{T}}\mu_n S_\theta C_\theta & e^{\mathrm{T}}\mu_n C_\theta^2\end{bmatrix}\begin{bmatrix}K^{\mathrm{T}}(C_\theta\dot{\theta}^2 + S_\theta\ddot{\theta}) \\ K^{\mathrm{T}}(S_\theta\dot{\theta}^2 - C_\theta\ddot{\theta})\end{bmatrix}\Bigg) \tag{64}$$

where,

$$M_p = \begin{bmatrix}m_{tot} + e^{\mathrm{T}}\mu_n S_\theta^2 e & -e^{\mathrm{T}}\mu_n S_\theta C_\theta e \\ -e^{\mathrm{T}}\mu_n S_\theta C_\theta e & m_{tot} + e^{\mathrm{T}}\mu_n C_\theta^2 e\end{bmatrix}. \tag{65}$$

Assembling the torque balance equation in (50) in multi-body matrix form as explained in [45] and [58] as

$$J\ddot{\theta} = D_o^{\mathrm{T}}\tau - S_\theta L A_o^{\mathrm{T}} h_X + C_\theta L A_o^{\mathrm{T}} h_Y + \tau_f. \tag{66}$$

Replacing the internal forces with the help of (61) and (62) along with (31) gives

$$\begin{aligned} J\ddot{\theta} = {} & D_o^{\mathrm{T}}\tau - S_\theta V(C_\theta\dot{\theta}^2 + S_\theta\ddot{\theta}) + S_\theta K(F_{fX} + F_{tX}) \\ & + C_\theta V(S_\theta\dot{\theta}^2 - C_\theta\ddot{\theta}) - C_\theta K(F_{fY} + F_{tY}) + \tau_f \end{aligned} \tag{67}$$

where V is given in (18) and τ_f is the N dimensional version of the values given in (48). Finally, joining the torque balance given in (67) and the translational motion equation given in (64) is expressed [11] as

$$\begin{aligned} & M_\theta\ddot{\theta} + W_\theta\dot{\theta}^2 + V_\theta\dot{\theta} + \Lambda_3|\dot{\theta}|\dot{\theta} - K_1\mu_n(S_\theta e\ddot{P}_X - C_\theta e\ddot{P}_Y) \\ & + S_\theta K(F_{DX} + F_{tX}) - C_\theta K(F_{DY} + F_{tY}) = D_o^{\mathrm{T}}\tau. \end{aligned} \tag{68}$$

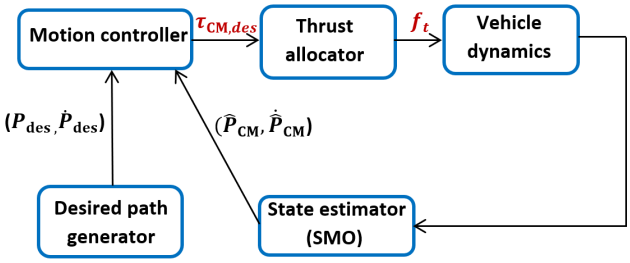

FIGURE 5. Schematic diagram of the basic vehicle control architecture.

where τ is the joint torque matrix and the multi-body matrices M_θ, W_θ, V_θ and K_1 are given in (20) - (27). Since the system modelling is completed, the design aspects of the controller and state observer are explained next.

III. CONTROL SYSTEM AND STATE OBSERVER DESIGN

The objective is to design a control system that drives the system states, including the position of the C.M and the heading of the vehicle, to the desired values in finite time in a robust way. This requires the system to produce control signals that produce the desired forces and moments that bring the system to the desired state. The basic schematic diagram of the control architecture is given in Fig. 5. The desired forces and moments are represented by modifying (58) as

$$\tau_{\mathrm{CM},des} = \begin{bmatrix}F_{\mathrm{CM},des} \\ M_{\mathrm{CM},des}\end{bmatrix} = \begin{bmatrix}e^{\mathrm{T}} & 0^{1\times N} \\ 0^{1\times N} & e^{\mathrm{T}} \\ e^{\mathrm{T}}S_\theta K & -e^{\mathrm{T}}C_\theta K\end{bmatrix}\begin{bmatrix}F_{tX} \\ F_{tY}\end{bmatrix}. \tag{69}$$

It can be shortened as follows

$$\tau_{\mathrm{CM},des} = T_c(\theta) f_t. \tag{70}$$

The thruster configuration matrix defined in (54) can be used to determine the individual thruster forces required to achieve the desired forces and moments.

A. SLIDING SURFACE DESIGN

The proposed control system is an improved form of Sliding Mode Control (SMC), and to begin with, a sliding surface must be defined. The basic idea of the sliding mode control is shown in Fig. 6. It should be defined such that when the sliding variable σ becomes zero, the system state variables converge to zero asymptotically. To do that, a proper error variable ($\tilde{P}$) has to be defined, which corresponds to the output for the translational motion of the vehicle as given in (71). It is taken as the location of the C.M (P_{CM}) of the vehicle. The error is defined as the difference between the desired position ($P_{\mathrm{CM},des}$) and the actual location of the vehicle C.M (P_{CM}).

$$\tilde{P}_1 = \tilde{P} = \begin{bmatrix}\tilde{P}_X \\ \tilde{P}_Y\end{bmatrix} = P_{\mathrm{CM}} - P_{\mathrm{CM},des} = \begin{bmatrix}P_X - P_{X,des} \\ P_Y - P_{Y,des}\end{bmatrix} \tag{71}$$

To drive the controlled system state trajectories into the sliding surface $\sigma = \dot{\sigma} = 0$, where the system characteristics satisfy the desired values, the sliding surface must be selected carefully. To have a relative degree equal to 1 for the control

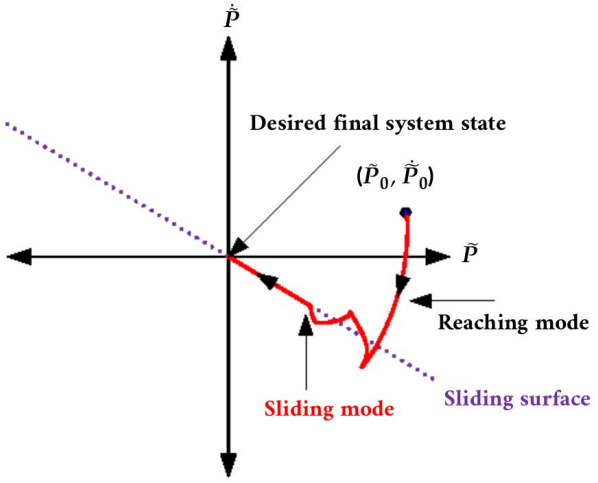

FIGURE 6. Schematic diagram illustrating the sliding mode control.

system, which is essential for the sliding mode control [11], the driving forces (F_{CM}) should appear in the first derivative of σ. As the analysis concentrates on the simulation results, the instantaneous position and velocity values from the sensors are not available. Hence, it is essential to evaluate these parameters with sufficient accuracy. Conventional integration methods have limited accuracy and reliability. So, it is decided to go with a sliding mode-based state observer where the position and velocity states are replaced by their estimated values $\hat{P}_1$ and $\hat{P}_2$ respectively, as explained in the next section. In this way, the updated sliding surface ($\hat{\sigma}$) is defined as

$$\hat{\sigma} = \begin{bmatrix}\hat{\sigma}_X \\ \hat{\sigma}_Y\end{bmatrix} = \lambda\hat{\tilde{P}} + \hat{\dot{\tilde{P}}} = \lambda\begin{bmatrix}\hat{\tilde{P}}_{1,X} \\ \hat{\tilde{P}}_{1,Y}\end{bmatrix} + \begin{bmatrix}\hat{\dot{\tilde{P}}}_{1,X} \\ \hat{\dot{\tilde{P}}}_{1,Y}\end{bmatrix}$$
$$= \lambda\begin{bmatrix}\hat{P}_{1,X} - P_{X,des} \\ \hat{P}_{1,Y} - P_{Y,des}\end{bmatrix} + \begin{bmatrix}\hat{P}_{2,X} - \dot{P}_{X,des} \\ \hat{P}_{2,Y} - \dot{P}_{Y,des}\end{bmatrix} \in \mathbb{R}^{2\times 1}. \quad (72)$$

Once the sliding variable values are obtained, it is used for estimating the control input. Before that, more details about the SMO observer are given below.

B. STATE OBSERVER DESIGN

As the analysis concentrates on the simulation results, accurate estimation of the system states is crucial. The states, including the position and velocity, can be estimated using the standard integration method from the instantaneous values, as seen in the literature [59]. But the reliability is minimal. Hence, an accurate integrator system based on a sliding mode system is designed. It is known as Sliding Mode state Observer (SMO) [44], [46] and is highly accurate for similar higher-order systems. The applicability of the same has been validated experimentally in [49]. The basic state observer is designed as follows.

$$\dot{\hat{P}}_1 = \begin{bmatrix}\dot{\hat{P}}_{1,X} \\ \dot{\hat{P}}_{1,Y}\end{bmatrix} = \begin{bmatrix}\hat{P}_{2,X} + z_{1,X} \\ \hat{P}_{2,Y} + z_{1.Y}\end{bmatrix} \quad (73)$$

$$\dot{\hat{P}}_2 = \begin{bmatrix}\dot{\hat{P}}_{2,X} \\ \dot{\hat{P}}_{2,Y}\end{bmatrix} = \begin{bmatrix}\hat{P}_{3,X} + z_{2,X} + \frac{1}{m_{tot}}F_{\text{CM},X} \\ \hat{P}_{3,Y} + z_{2,Y} + \frac{1}{m_{tot}}F_{\text{CM},Y}\end{bmatrix} \quad (74)$$

$$\dot{\hat{P}}_3 = \begin{bmatrix}\dot{\hat{P}}_{3,X} \\ \dot{\hat{P}}_{3,Y}\end{bmatrix} = \begin{bmatrix}z_{3,X} \\ z_{3,Y}\end{bmatrix} = \begin{bmatrix}k_3 sgn(e_{1,X}) \\ k_3 sgn(e_{1,Y})\end{bmatrix} \quad (75)$$

The z terms are defined as follows.

$$z_1 = \begin{bmatrix}z_{1,X} \\ z_{1,Y}\end{bmatrix} = \begin{bmatrix}k_1|e_{1,X}|^{2/3}sgn(e_{1,X}) \\ k_1|e_{1,Y}|^{2/3}sgn(e_{1,Y})\end{bmatrix} \quad (76)$$

$$z_2 = \begin{bmatrix}z_{2,X} \\ z_{2,Y}\end{bmatrix} = \begin{bmatrix}k_2|e_{1,X}|^{1/3}sgn(e_{1,X}) \\ k_2|e_{1,Y}|^{1/3}sgn(e_{1,Y})\end{bmatrix} \quad (77)$$

$$z_3 = \begin{bmatrix}z_{3,X} \\ z_{3,Y}\end{bmatrix} = \begin{bmatrix}k_3 sgn(e_{1,X}) \\ k_3 sgn(e_{1,Y})\end{bmatrix} \quad (78)$$

k_1, k_2 and k_3 are the gains which are selected according to [44] and [11] as

$$k_1 = 6L_c^{1/3},\ k_2 = 11L_c^{1/2},\ k_3 = 6L_c. \quad (79)$$

where L_c has to be a large constant which will be selected in section V. Note that the observer error values (e) are defined as

$$e_1 = P - \hat{P}_1, \quad e_2 = \dot{P} - \hat{P}_2, \quad e_3 = F(t) - \hat{P}_3. \quad (80)$$

The external disturbance variable $F(t)$ is defined in (93). The error dynamics of the state observer is given as follows, and the stability analysis of the same will be carried out in the next section.

$$\Sigma_e = \begin{cases}\dot{e}_1 = -k_1|e_1|^{2/3}sgn(e_1) + e_2 \\ \dot{e}_2 = -k_2|e_1|^{1/3}sgn(e_1) + e_3 \\ \dot{e}_3 = -k_3 sgn(e_1) + \dot{F}(t)\end{cases} \quad (81)$$

C. CONTROL INPUT ESTIMATION

The essential details of control equations of the Super Twisting Algorithm (STA) with adaptive gains [11], [15], which is used in this paper, are explained here. The output of this control system will be used to find the desired force and moment values. The control input values are obtained by substituting the $\hat{\sigma}$ in the following equation.

$$u_{\text{STA}} = \begin{bmatrix}u_X \\ u_Y\end{bmatrix} = \begin{bmatrix}-\alpha_X|\hat{\sigma}_X|^{1/2}sgn(\hat{\sigma}_X) + \nu_X \\ -\alpha_Y|\hat{\sigma}_Y|^{1/2}sgn(\hat{\sigma}_Y) + \nu_Y\end{bmatrix} \quad (82)$$

where,

$$\begin{bmatrix}\dot{\nu}_X \\ \dot{\nu}_Y\end{bmatrix} = \begin{bmatrix}-\beta_X sgn(\hat{\sigma}_X) \\ -\beta_Y sgn(\hat{\sigma}_Y)\end{bmatrix} \quad (83)$$

$$\begin{bmatrix}\dot{\alpha}_X \\ \dot{\alpha}_Y\end{bmatrix} = \begin{bmatrix}\begin{cases}\omega_1\sqrt{\frac{\gamma_1}{2}}, & \text{if } |\hat{\sigma}_X| > \alpha_m \\ 0, & \text{if } |\hat{\sigma}_X| \le \alpha_m\end{cases} \\ \begin{cases}\omega_1\sqrt{\frac{\gamma_1}{2}}, & \text{if } |\hat{\sigma}_Y| > \alpha_m \\ 0, & \text{if } |\hat{\sigma}_Y| \le \alpha_m\end{cases}\end{bmatrix} \quad (84)$$

$$\begin{bmatrix}\beta_X \\ \beta_Y\end{bmatrix} = \begin{bmatrix}2\epsilon\alpha_X + \lambda + 4\epsilon^2 \\ 2\epsilon\alpha_Y + \lambda + 4\epsilon^2\end{bmatrix} \quad (85)$$

where ϵ, λ, γ_1 and ω_1 are positive constants. For implementation purposes, a small boundary (α_m), as shown in Fig. 7,

is applied to the sliding surface, which can be expressed as (86). This facilitates expressing the adaptive gains as suggested in [49]. To achieve the asymptotic convergence of state variables, it is important for the sliding variable $\hat{\sigma}$ to become zero in finite time with the help of the driving force F_{CM}. Therefore, it must be chosen so that the STA control output u_{STA} occurs in the equation of the sliding variable's first derivative [41]. In another way, it is desired to have the derivative of the sliding parameter as $\dot{\hat{\sigma}} = u_{\mathrm{STA}}$. To get that, taking the time derivative of (72) and by substituting $\dot{\hat{P}}_1$ and $\dot{\hat{P}}_2$ defined in (73) - (75) as shown below.

$$\dot{\hat{\sigma}} = (\dot{\hat{P}}_1 - \dot{P}_{des}) + (\dot{\hat{P}}_2 - \ddot{P}_{des}) = (\hat{P}_2 + z_1 - \dot{P}_{des}) + (\hat{P}_3 + z_2 + \frac{1}{m_{tot}} F_{\mathrm{CM},des} - \ddot{P}_{des}) \quad (86)$$

If $F_{\mathrm{CM},des}$ is selected as

$$F_{\mathrm{CM},des} = m_{tot}(-\hat{P}_2 - z_1 + \dot{P}_{des} - \hat{P}_3 - z_2 + \ddot{P}_{des} + u_{\mathrm{STA}}) \quad (87)$$

This will give the required result as

$$\dot{\hat{\sigma}} = u_{\mathrm{STA}}. \quad (88)$$

Thus, the net control thrust has to be calculated as per (87) for the asymptotic convergence of state variables. Before carrying out the simulation, the entire system's stability has to be analysed in the next step.

IV. STABILITY ANALYSIS

In this section, the stability of the closed-loop system is analysed. The objective is to prove that the tracking error converges to zero asymptotically as long as (87) is satisfied. Firstly, the state error variables will be introduced, followed by the overall closed-loop dynamics and subsystem-wise stability analysis.

A. STATE ERROR VARIABLES

Equation (63) can be rewritten as

$$\ddot{P} = \begin{bmatrix} \ddot{P}_X \\ \ddot{P}_Y \end{bmatrix} = \begin{bmatrix} \frac{1}{m_{tot}}(e^{\mathrm{T}} F_{fX} + F_{\mathrm{CM},X}) \\ \frac{1}{m_{tot}}(e^{\mathrm{T}} F_{fY} + F_{\mathrm{CM},Y}) \end{bmatrix} \quad (89)$$

$e^{\mathrm{T}} F_{fX}$ is the vector sum of all fluid forces along the X direction, and similarly, $e^{\mathrm{T}} F_{fY}$ is the vector sum of all fluid forces along the Y direction. Since these forces vary continuously with respect to time, they can be represented as $f(t)$. Note that the values of $f(t)$ and $\dot{f}(t)$ are always bounded as they are determined by the physical forces acting on the vehicle, which are always finite values [53], [60]. Thus,

$$\ddot{P} = \begin{bmatrix} \ddot{P}_X \\ \ddot{P}_Y \end{bmatrix} = \begin{bmatrix} \frac{1}{m_{tot}}(f_X(t) + F_{\mathrm{CM},X}) \\ \frac{1}{m_{tot}}(f_Y(t) + F_{\mathrm{CM},Y}) \end{bmatrix} \quad (90)$$

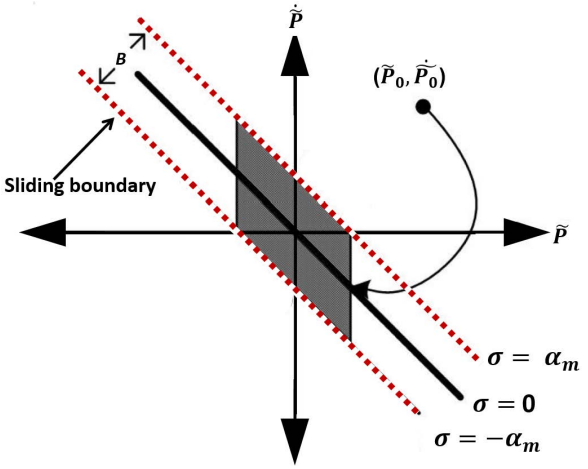

FIGURE 7. Schematic diagram illustrating the sliding boundary.

The position error variable introduced in (71) is restructured as follows.

$$\dot{\tilde{P}}_1 = \dot{\tilde{P}} = \tilde{P}_2 \quad (91)$$

$$\dot{\tilde{P}}_2 = \ddot{\tilde{P}} = \ddot{P} - \ddot{P}_{des} = \frac{1}{m_{tot}}(f(t) + F_{\mathrm{CM}}) - \ddot{P}_{des} \quad (92)$$

The external fluid force $f(t)$ and the desired acceleration vector $\ddot{P}_{des}$ are combined to form the new function $F(t)$ as follows.

$$F(t) = \frac{1}{m_{tot}} f(t) - \ddot{P}_{des} \quad (93)$$

Thus, the updated error variables can be written as

$$\dot{\tilde{P}}_1 = \tilde{P}_2 \quad (94)$$

$$\dot{\tilde{P}}_2 = F(t) + \frac{1}{m_{tot}} F_{\mathrm{CM}} \quad (95)$$

Note that $F(t)$ and $\dot{F}(t)$ are bounded as they are made from two bounded variables.

B. SYSTEM CLOSED-LOOP DYNAMICS

By using $\hat{P}_1 = P - e_1$ and that $\hat{P}_2 = \dot{P} - e_2$ as per (80), $\lambda = 1$, the sliding variable given in (72) can be written as

$$\hat{\sigma} = (P - e_1 - P_{des}) + (\dot{P} - e_2 - \dot{P}_{des}). \quad (96)$$

By using the relations

$$\tilde{P}_1 = P - P_{des} \quad \tilde{P}_2 = \dot{\tilde{P}}_1 = \dot{P} - \dot{P}_{des} \quad (97)$$

(96) can be written as

$$\hat{\sigma} = \tilde{P}_1 + \dot{\tilde{P}}_1 - e_1 - e_2. \quad (98)$$

Using the above equation along with (82) and (88), the overall system closed loop dynamics can be written as

$$\Sigma_s = \begin{cases} \dot{\hat{\sigma}} = -\alpha |\hat{\sigma}|^{1/2} sgn(\hat{\sigma}) + \nu \\ \dot{\nu} = -\beta sgn(\hat{\sigma}) \\ \dot{\tilde{P}}_1 = \hat{\sigma} - \tilde{P}_1 + e_1 + e_2 \end{cases} \quad (99)$$

For ease of analysis, the full system Σ_s is further divided into subsystems Σ_{s1} and Σ_{s2} as follows.

$$\Sigma_{s1} = \begin{cases} \dot{\hat{\sigma}} = -\alpha|\hat{\sigma}|^{1/2} sgn(\hat{\sigma}) + \nu \\ \dot{\nu} = -\beta sgn(\hat{\sigma}) \end{cases} \tag{100}$$

$$\Sigma_{s2} = \left\{ \dot{\tilde{P}}_1 = \hat{\sigma} - \tilde{P}_1 + e_1 + e_2 \right. \tag{101}$$

Both these subsystems, along with the SMO error dynamics (Σ_e) defined in (81), will be analysed separately as follows.

C. SUBSYSTEM WISE STABILITY ANALYSIS

1) ANALYSIS OF Σ_{s1}

This subsystem has the structure of STA with adaptive gains, and it is not affected by Σ_e, as clear from (101). A Lyapunov function for systems with this structure is proposed in [41] by applying the STA with adaptive gains given in (84), where $\epsilon, \lambda, \gamma_1$ and ω_1 are arbitrary positive constants, it is proved to be a Lyapunov function for subsystem Σ_{s1} and that for any initial conditions, it reaches the desired sliding surface in finite time. Thus, as per the literature, the subsystem is Uniform Global Asymptotic Stable (UGAS) as long as (87) is satisfied. This also implies that

$$|\hat{\sigma}(t)| \leq \beta_1 \quad \forall\, t \geq 0. \tag{102}$$

Note that β_1 is the upper bound for the sliding variable value.

2) ANALYSIS OF Σ_e

This subsystem is the standard error dynamics for the SMO system. In [61], a radially unbounded and positive definite Lyapunov function for a third-order observer is presented. It is demonstrated that it suits as a Lyapunov function for subsystem Σ_e, whose trajectories converge in finite time to the origin $e = 0$ given that $F(t)$ given in (93) is bounded. Since the condition is valid here, as previously mentioned, the origin is globally finite time stable for all values of $F(t)$. It indicates that the origin is UGAS for Σ_e as per propositions 2 and 3 given in [62] about the asymptotic stability of the dynamic systems. It implies that

$$|e(t)| \leq \beta_2 \quad \forall\, t \geq 0. \tag{103}$$

Note that the β_2 is the upper bound for the error values.

3) ANALYSIS OF Σ_{s2}

Unlike the two previous subsystems, it is not a generic equation that is well-verified to be stable in the literature. To analyse the stability of this subsystem, a Lyapunov function is defined as follows.

$$V_{s2}(\tilde{P}) = \frac{1}{2}\tilde{P}_1^{\,2} \tag{104}$$

The stability analysis needs to evaluate the boundedness of $\tilde{P}_1$ even in the worst-case scenario, such as when $e_1 \neq 0$ and $e_2 \neq 0$ to ensure the global boundedness of the system. It should be noted that the boundedness of $\hat{\sigma}$ and $e(t)$ are given by β_1 and β_2 respectively as per (102) and (103). The derivative of the Lyapunov function in (104) is given by

$$\begin{aligned} \dot{V}_{s2}(\tilde{P}) = \tilde{P}_1\dot{\tilde{P}}_1 &= -|\tilde{P}_1|^2 + (\hat{\sigma} + e_1 + e_2)\tilde{P}_1 \\ &\leq -|\tilde{P}_1|^2 + \theta|\tilde{P}_1|^2 - \theta|\tilde{P}_1|^2 + (\beta_1 + 2\beta_2)|\tilde{P}_1| \\ &\leq -(1-\theta)|\tilde{P}_1|^2 \quad \forall\ |\tilde{P}_1| \geq \frac{\beta_1 + 2\beta_2}{\theta}. \end{aligned} \tag{105}$$

Where θ is always a positive number with $0 < \theta < 1$, meaning the function $(1-\theta)|\tilde{P}_1|^2$ is always positive definite. Then the solutions are Uniformly Globally Bounded (UGB) because the conditions for Lyapunov stability theorem 4.18 given in [63] are satisfied (see Appendix: Theorem 1). Thus combining Σ_{s1}, Σ_{s2} and Σ_e, the entire system is proved to be UGAS as the conditions of Lemma 2.1 given in [64] are satisfied (see Appendix: Theorem 2). Since the stability analysis is completed, the simulation methodology is explained next.

TABLE 2. Hull number on which various thrusters attached.

Configuration	Surge thruster	Heave thruster	Sway thrusters
A	11	6	2 4 8 10
B	11	6	3 5 7 9
C	11	6	2 5 7 10

V. SIMULATION METHODOLOGY

The mathematical model of the vehicle, along with the force allocation matrix and the controller designed in the previous section, are implemented for the simulation in MATLAB [65]. The proposed vehicle has $N = 11$ hulls, each measuring $2L = 0.27$ m in length and $m_i = 2.1$ kg in mass. The hull section with major and minor diameters of $a = b = 0.05$ m was evaluated for the hydrodynamic-related parameters $C_t, C_n, \lambda_1, \lambda_2$ and λ_3. The equations derived in (52) are used to compute the updated fluid coefficients using $C_{f0} = 0.03, C_{D0} = 1$, and the assumption that the density of the water to be $\rho = 1000\ kg/\mathrm{m}^3$ is used as well. The initial point of the C.M is selected as $P_{\mathrm{CM},0} = [0, 0]$ m. The control parameters are selected as $\epsilon = 1$, $\gamma_1 = 1$, $\lambda = 1$, $\omega_1 = 8$ and $\alpha_m = 0.05$ from literature [11]. The observer gain parameter L_c selected must be suitably large, as explained in section III-B. For the simulations, it is manually tuned to provide good performance as $L_c = 50$. Compared to the tuning process of other conventional controllers (say PD), the choice of control parameters is not crucial because the STA has an adaptive gain. Although it will always drive the system to the desired value, the speed at which it does so might be affected by the gain value selected. It is decided to set the sliding parameter (λ) value to 1, and a fixed-step solution with a fixed step size of 10^{-5} was employed for the simulations. The applied thruster configurations are A, B and C, as described in Table 2. It features four sway thrusters capable of exerting forces normal to the hulls and the surge thrusters attached to hull number N, which exerts a force along the hull's x-axis. Note that thrusters are numbered from the rear, meaning thruster 5 is the axial thruster on the 11^{th}

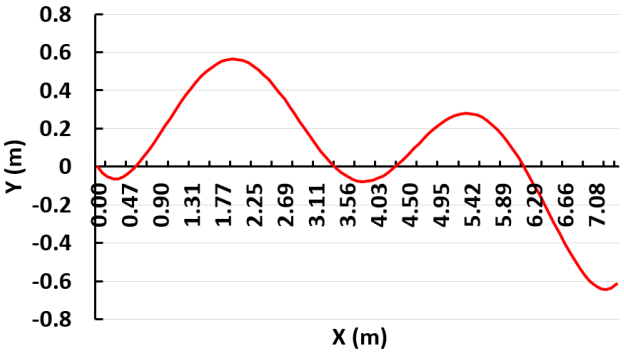

FIGURE 8. Schematic diagram illustrating the desired path.

hull. Also, thrusters 2 and 3 are considered as inner thrusters, and the remaining are considered as outer thrusters. As the proposed operation is purely in the *XY* plane, heave thrusters on the middle hull are not operated but are considered for the control system. The operation modes of the vehicle are explained next.

A. OPERATION MODES OF THE VEHICLE

Split-hull underwater vehicles can operate in different modes due to their flexible configuration. The proposed vehicle is mainly designed for two operation modes: Torpedo and Inspection. The vehicle has to track a desired trajectory in both cases, and Fig. 8 shows the desired trajectory used for the tracking problem. Torpedo mode is where all hulls are aligned with zero joint angles, making the vehicle look like a single-hull torpedo AUV. This mode is suitable for long-distance travel where minimal fluid resistance and completion time are crucial such as water body mapping. The snapshots of the torpedo mode operation are shown in Fig. 9, where the vehicle is tracing the desired trajectory. Manoeuvrability is limited and unsuitable for underwater intervention tasks because it does not use joint control for flexible multi-body movements. For that, inspection mode is used, during which the vehicle uses the potential of its flexible body where the hulls have different orientations to conduct the desired inspection. To do that, the joint angles are constantly adjusted to meet the operation requirement. In this paper, a typical case of the inspection mode is considered where the head of the vehicle is aligned in a different direction while the overall C.M of the vehicle has to track the desired trajectory, and Fig. 11 illustrates the same. The desired heading is changed every 10 seconds for the simulation, as explained in Fig. 11. The operation with this kind of orientation of the hulls will create massive disturbances to the C.M of the vehicle that needs to be compensated by the thrust forces, making the thrust force requirement in inspection mode significantly higher than the torpedo mode. Thus, the control system has two tasks: The first is to control the heading to the desired value; the second is to ensure that the vehicle C.M traces the desired trajectory by adjusting the thruster forces and joint angles. The basic concepts of heading control are explained next.

TABLE 3. Thrust distribution modes and the weight values.

Weight mode	W_1	W_2	W_3	W_4	W_5
1	1	1	1	1	1
2	2	1	1	1	1
3	1.5	1	1	1.5	1.5
4	2	1	1	2	2
5	3	1	1	3	3
6	4	1	1	4	4
7	5	1	1	5	5
8	1/5	1	1	1/5	1/5
9	1/4	1	1	1/4	1/4
10	1/3	1	1	1/3	1/3
11	1/2	1	1	1	1
12	1/2	1	1	1/2	1/2
13	1/1.5	1	1	1/1.5	1/1.5
14	$1/((l_{\tau i}+10^{-9})/10L))$				
15	$1/(1+l_{\tau i}/10L)$				
16	$1/exp((l_{\tau i}+10^{-9})/10L)$				
17	$1/exp(1+l_{\tau i}/10L)$				
18	$1/((l_{\tau i}+10^{-9})/10L))$				1
19	$1/(1+l_{\tau i}/10L)$				1
20	$1/exp((l_{\tau i}+10^{-9})/10L)$				1
21	$1/exp(1+l_{\tau i}/10L)$				1

B. DESIRED HEADING OF THE VEHICLE

In general, the heading is determined by the vehicle's orientation during the operation. When it comes to split-hull underwater vehicles, it is taken as the average orientation of individual hulls, as seen in the literature [8], [48]. Still, its definition can depend on the objectives of the vehicle considered. The main objective of most existing split-hull underwater vehicles is to trace the desired trajectory. As part of that, it needs to be made sure that the average orientation is along the desired heading and the C.M is following the desired trajectory. This paper also validates this when the vehicle is operating in torpedo mode. However, as the vehicle is also designed for inspection operation, situations, where the leading hull is facing a different orientation inspecting while the C.M is tracing the desired trajectory can arise. So, the heading is defined as the orientation of the leading hull (N^{th}) in this paper. This means the control system has to handle the trajectory tracking problem while maintaining the desired heading of the leading hull. The conventional Line Of Sight (LOS) based algorithm is used for the torpedo mode heading control, which periodically updates the desired heading data to the control system. LOS is a very popular heading control algorithm used for marine vehicles. It is defined as given in (106), and the corresponding graphical illustration is given in Fig. 10. The parameter Δ is the Look-Ahead distance that decides the convergence rate to the desired path. This paper takes it as 2 m, which is a value less than the vehicle length of 3 m.

$$\theta_{des} = -\arctan(\frac{\Delta_Y}{\Delta}), \quad \Delta > 0 \tag{106}$$

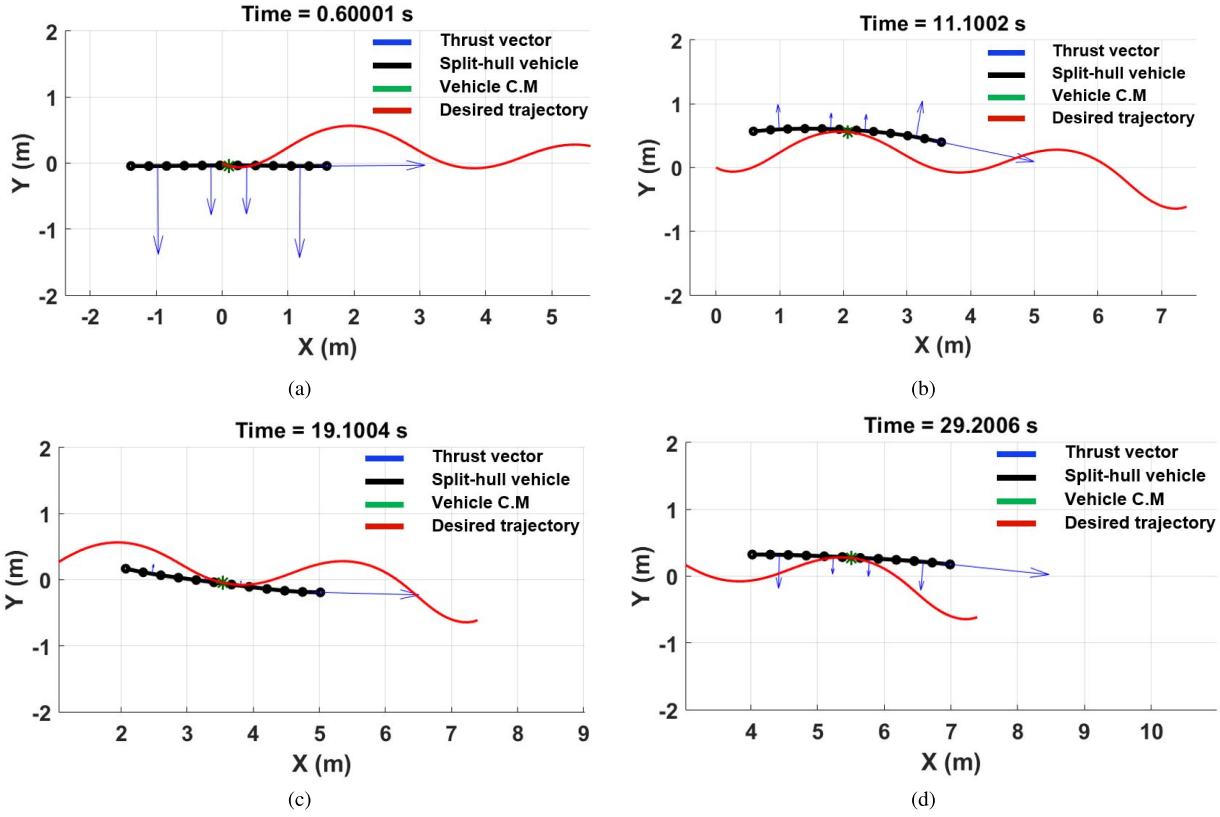

FIGURE 9. Snapshots of the simulation of torpedo mode operation.

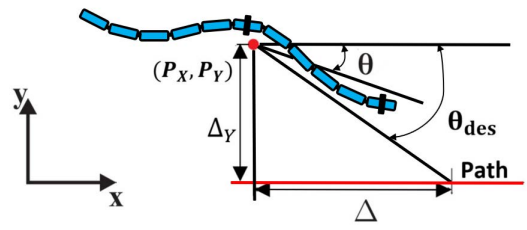

FIGURE 10. Schematic diagram illustrating the LOS algorithm.

Regarding the inspection mode, the leading hull follows the desired heading while the remaining hulls follow the wave-like joint angle pattern proposed in [8] as follows.

$$\phi_{ij,des} = A\sin(\omega t + (i-1)\delta) + \phi_0, \quad j = i+1,\ i \in [1, .., N-2] \tag{107}$$

$$\phi_0 = \theta_N - \theta_{des} \tag{108}$$

A represents the amplitude of the joint angle, ω is the angular frequency of the sinusoidal joint motion, which is zero in this case, δ defines the phase shift between the individual joints, and ϕ_0 is the joint offset used to control the overall heading of the vehicle. Joint angles in (107) ensure that the hulls align in a sinusoidal pattern such that the C.M tracks the desired trajectory and the leading hull maintains the desired trajectory. Note that the -ve term for the θ_{des} in (108) is because the heading reference is given to the leading N^{th} hull. The wave pattern is selected as $A = 30°,\ \omega = 70°,\ \delta = 40°$ here.

C. DYNAMIC THRUST DISTRIBUTION

Unlike previous studies [11], [49], where a fixed and equal weight was given to all thrusters to minimise power consumption, a dynamic weight allocation is proposed and implemented in this paper. The basic idea is that thrusters that are far from the C.M have higher moment effects than the ones closer. This means that the outer thrusters are far more effective in controlling the vehicle orientation than the inner ones. To do that, a set of possible weight values are considered as given in Table 3 where a new matrix is introduced called moment vector, which is defined as

$$l_\tau = abs(e^{\mathrm{T}}(S_\theta K B_X^{\mathrm{T}} - C_\theta K B_Y^{\mathrm{T}})) \quad \in \mathbb{R}^{1\times r} \tag{109}$$

It has r elements, which correspond to the number of thrusters. It is derived from (54) and, geometrically, it is the magnitude of the moment vector of the thruster on the vehicle C.M which is equal to the effective perpendicular distance between the thrust vector and the C.M of vehicle. B_X and B_Y contribute to the instantaneous orientation of the thruster as given in (54) whereas the terms $S_\theta K$ and $C_\theta K$ handles the overall vehicle orientation. To normalise the values, l_τ is divided by $10L$ for the modes from 14 to 21, which is the maximum possible moment vector length of the outermost

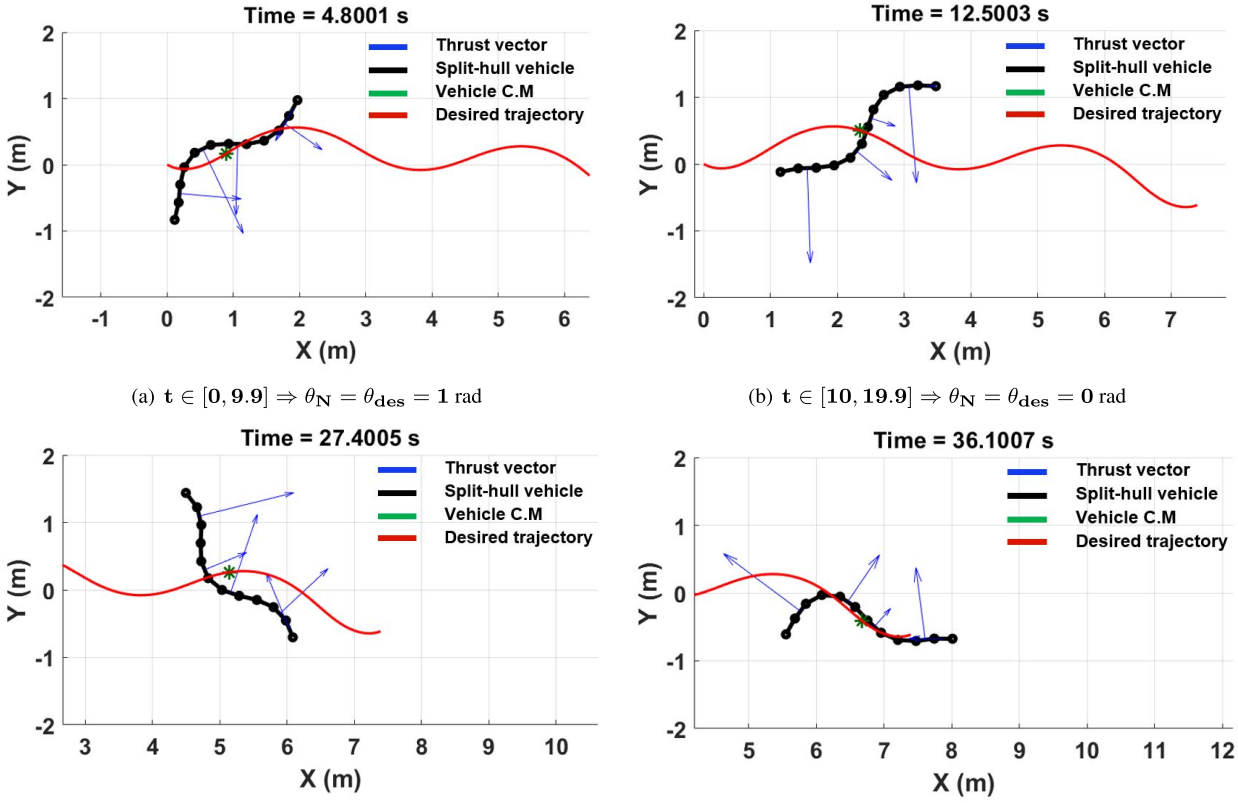

(a) $\mathbf{t} \in [\mathbf{0}, \mathbf{9.9}] \Rightarrow \theta_{\mathbf{N}} = \theta_{\mathbf{des}} = \mathbf{1}$ rad

(b) $\mathbf{t} \in [\mathbf{10}, \mathbf{19.9}] \Rightarrow \theta_{\mathbf{N}} = \theta_{\mathbf{des}} = \mathbf{0}$ rad

(c) $\mathbf{t} \in [\mathbf{20}, \mathbf{29.9}] \Rightarrow \theta_{\mathbf{N}} = \theta_{\mathbf{des}} = -\mathbf{1}$ rad

(d) $\mathbf{t} \in [\mathbf{30}, \mathbf{39.9}] \Rightarrow \theta_{\mathbf{N}} = \theta_{\mathbf{des}} = \mathbf{0}$ rad

FIGURE 11. Snapshots of the simulation of inspection mode operation.

thrusters (1 and 5). Note that the denominator of mode 14, $((l_{\tau i} + 10^{-9})/10L)$ is limited to a maximum value of 1, whereas that of mode 15, $(1 + l_{\tau i}/10L)$ ranges from 1 to 2. Corresponding exponential values are taken for modes 16 and 17, where the denominator values range from 1 to 2.718 for the former and from 2.718 to 7.38 for the latter. The importance of determining the denominator values is explained in section VI-B. For the modes from 18 to 21, unit weight was given to the thruster five as it is an axial one, while all other weights are kept the same as 14 to 17. Now, the simulations are carried out with these weight modes, as explained below.

VI. RESULTS

A. SYSTEM WITH REGULAR UNIT THRUST DISTRIBUTION

Before going into the proposed adaptive thrust distribution, the regular unit thrust weight distribution (mode 1) is applied to both torpedo and inspection modes for configuration C to check the effectiveness of the control system and the state observer.

1) UNIT THRUST WEIGHT DISTRIBUTION ON TORPEDO MODE

The simulation is carried out first using equal weight distribution for the torpedo operation, and the results are shown in Fig. 12. The parameters are selected in section V, and weights are selected as per mode 1 given in Table 3 to give equal unit weights for the thrusters. During the torpedo mode operation of the vehicle, as shown in Fig. 9 (a) - (d), the desired joint angles are set to zero, and the heading of the leading hull is controlled as per (108). The same figure also shows the location of vehicle C.M, which is the point of interest for the trajectory tracking problem. Variations in the X and Y coordinates of the C.M are shown in 12 (a) and (b), and the corresponding variation in the position error values are shown in Fig. 12 (c). The maximum errors in X and Y directions are limited to 0.0148 m and 0.0072 m, respectively, occurring in the initial time until $t = 4$ s and error values are almost zero in the remaining period. The variation in the thrust values is shown in Fig. 12 (d), where both X and Y components of the net thrust are given. Note that this is the net desired thrust that has to be provided by the combined action of all thrusters, not by a single thruster. The maximum desired thrust is capped at 150 N from a safety point of view, though the estimated values are always below 120 N throughout the operation. Also, the individual thrust values are capped at 48 N to account for the thruster limitation. However, the desired individual thrust values are always below 35 N when calculated as per (70). In addition to the control system, the performance of the SMO is evaluated. To do that, the observer error values e_1 and e_2 are evaluated and shown in Fig. 12 (e) and (f), respectively. It is

seen that the maximum error values are in the 10^{-7} m range for the position estimate ($\hat{P}_1$) and in the 10^{-4} m/s range for the velocity estimator ($\hat{P}_2$). It is important to note that these error values are negligible compared to the dimensions of the vehicle and trajectory used.

2) UNIT THRUST WEIGHT DISTRIBUTION ON INSPECTION MODE

Similar to the torpedo mode, the simulation is carried out using equal weight distribution for the inspection mode, and the results are shown in Fig. 13. The parameters are selected in section V, and weights are selected as per mode 1 given in Table 3 to give equal unit weights for the thrusters. During the inspection operation of the vehicle, as shown in Fig. 11 (a) - (d), the heading of the leading hull is changed every 10 s and the overall orientation of the vehicle changes in a sinusoidal wave pattern. The same figure also shows the location of vehicle C.M, which is the point of interest for the trajectory tracking problem. Note from the figure that the orientations of the different hulls are adjusted as per (107) to ensure that vehicle C.M is tracking the desired trajectory. Variations in the X and Y coordinates of the C.M are shown in 13 (a) and (b), and the corresponding variation in the position error values are shown in Fig. 13 (c). The maximum errors in X and Y directions are limited to 0.019 m and 0.01 m, respectively, and it happens in the initial time until $t = 3$ s. In the remaining period, error values are negligible except for the minor spikes occurring at $t = 10$ s, 20 s and 30 s due to the sudden change in the desired heading of the vehicle. The variation in the thrust values is shown in Fig. 13 (d), where both X and Y components of the net thrust are given. Similar to the position error case, there are spikes at the $t = 10$ s, 20 s and 30 s, and the values are always below 150 N during the operation. Note that this desired thrust has to be provided by the combined action of all thrusters. It is where the optimised thrust distribution concept is implemented, and more about that will be explained in the next section. In addition to the control system, the performance of the SMO is also evaluated. To do that, the observer error values e_1 and e_2 are evaluated and shown in Fig. 13 (e) and (f), respectively. It is seen that the maximum error values are in the 10^{-7} m range for the position estimate ($\hat{P}_1$) and in the 10^{-4} m/s range for the velocity estimator ($\hat{P}_2$). Though these error values are slightly higher than that for the torpedo mode, they exist only at the spikes during the change in vehicle orientation; otherwise, they settle to zero. This excellent performance from the observer is expected as SMO is proved to be highly accurate for similar dynamic non-linear systems as per the previous studies [44], [46], [49].

B. SYSTEM WITH ADAPTIVE THRUST DISTRIBUTION

As a continuation of the unit thrust weight distribution work, different thrust weight values are applied to the system during torpedo and inspection modes as given in Table 3. The new weights include 2, 3, 4 and 5, and their corresponding inverses replace the previous unit values. They are given to the outer thrusters (1, 4 and 5) while keeping the unit weights to the inner ones (2 and 3). There are 21 weight distribution modes, and the modes from 1 to 7 give higher weights to the outer thrusters. The lower weights are applied to the same thrusters by selecting the corresponding inverse values as given in modes 7 - 13. Note that the weights are kept constant throughout the simulation until mode 13. Modes 2 and 11 are used to check the effect of weight mode on the thruster usage. The weights (W) of 2 and 1/2, respectively, are given to thruster 1, with unit weights on the remaining thrusters. Simulations are carried out with these weight modes for both inspection and torpedo modes, and the results are shown in Fig. 14. It is clear that the higher the weight given to a thruster, the lower the thrust usage and vice versa. This is understandable from (60), where thrust values are directly related to the inverse of weight (W^{-1}) applied. Though there is a multiplier of W in the same equation, multiplication with T_c reduces its net effect, as visible from the results. Based on these findings, the remaining weight modes in Table 3 are applied to the system, and the simulations for both torpedo and inspection modes are carried out as follows.

1) ADAPTIVE THRUST DISTRIBUTION ON TORPEDO MODE

Similar to the unit thrust weight distribution case, various weight modes are applied to the torpedo operation for the thruster configurations A, B and C. The results are shown in Fig. 15. The mean value of the overall thruster usage is calculated for each mode and is given in Fig. 15 (a). It is observed that all configurations have an almost similar trend, with mode 15 having the lowest and mode 7 having the highest values. Also, configuration C has the lowest mean thrust usage at 4.08 N, whereas B has the highest one at 4.2 N. Same trend is observed with the peak mean thrust usage, where C is at 4.42 N and B is at 4.53 N. It shows the advantage of having individual thrusters located farther in C than B, where the thrusters are closely located. Another interesting observation is that the higher the weight given to the outer thrusters, the higher the overall average thrust usage, which is visible from the rise in the graph from modes 1 to 7. Similarly, when a lower thrust weight is given to the outer thrusters, as with modes from 8 to 20, the overall mean thrust usage gets reduced. For a given operation, higher weights given to the outer thrusters result in lower usage of the same thrusters and higher usage of the inner thrusters. This results in higher overall thrust usage as the latter thrusters have a lower moment effect on the vehicle C.M than the former ones. Due to this reason, modes after 7 use the outer thrusters more and hence have lower overall average thrust usage. It is also observed that the mean thrust usage is the lowest for mode 15, where the denominator value varies from 1 to 2. The figure also shows that the second lowest value corresponds to mode 16, where the denominator ranges between 1 and 2.718, which overlaps partly with mode 15. In addition to the mean thrust values, the variation in the thruster usage is also calculated and shown with the help of the thrust variance graph shown in Fig. 15 (b). The variance increases from an average value of

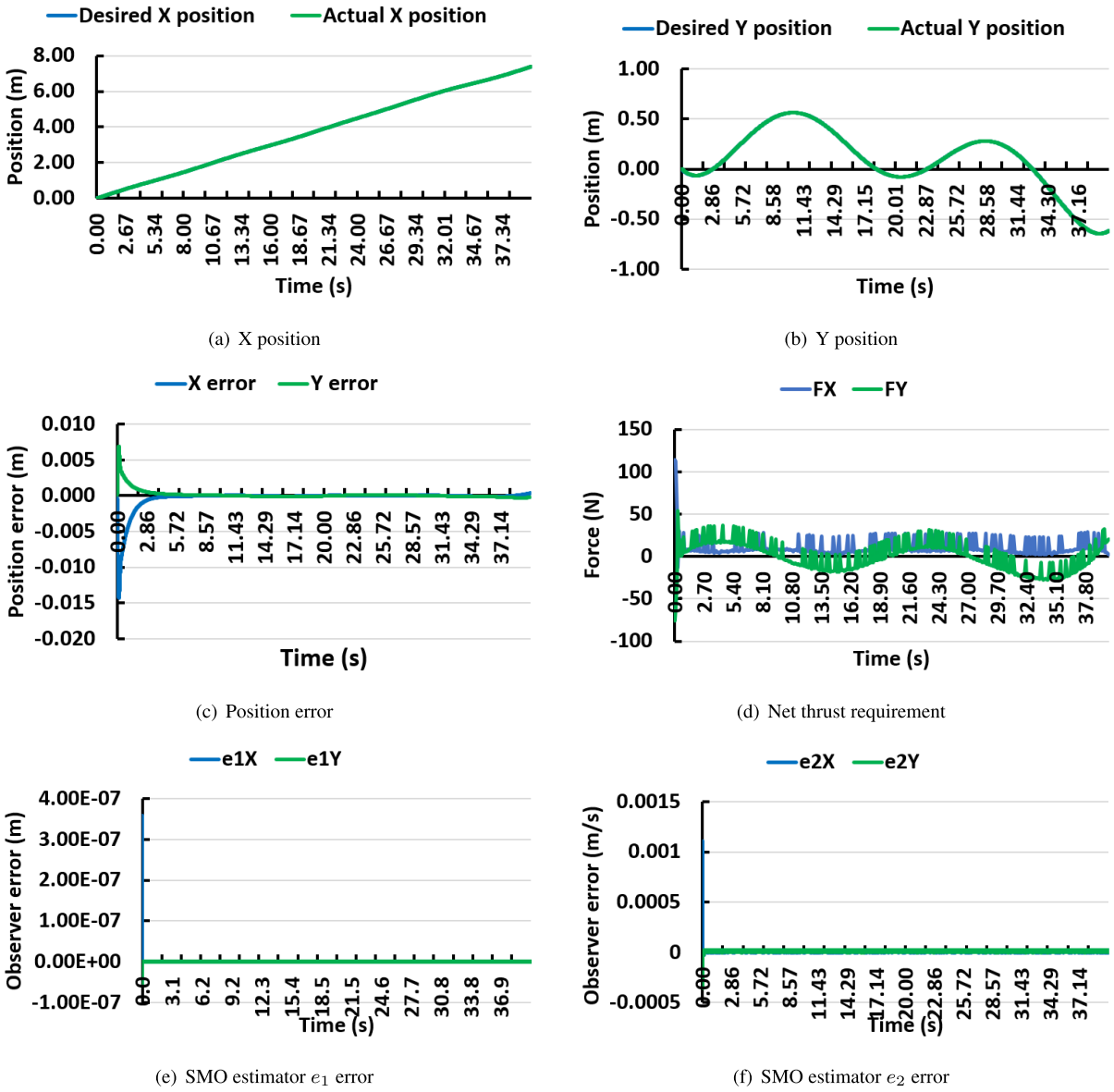

(a) X position

(b) Y position

(c) Position error

(d) Net thrust requirement

(e) SMO estimator e_1 error

(f) SMO estimator e_2 error

FIGURE 12. Variation of different parameters with torpedo mode operation.

134 at mode 1 to 190 at mode 7 and then goes down to a steady lower value comparable to mode 1. This shows that higher weight given to the outer thrusters causes increased variation in the overall thrust values. Thus, choosing a lower weight for the outer thrusters favours both mean thrust usage and thrust variation. When modes from 18 to 21 are considered where a unit weight is given to thruster 5 (surge thruster), the mean thrust usage is better than the regular mode 1; however, it performs inferior compared to the corresponding 14 to 17 modes.

2) ADAPTIVE THRUST DISTRIBUTION ON INSPECTION MODE

Similar to the previous case with torpedo mode, different weight modes are applied to the inspection operation for the thruster configurations A, B and C. The results are shown in Fig. 16. The mean value of the thruster usage is calculated for each mode and are given in Fig. 16 (a), and it is observed that similar to the case on torpedo mode, all configuration have similar trend with mode 7 having the highest thrust usage and mode 15 having the lowest one. The rise in the graph from modes 1 to 7 indicates that the overall average thrust usage increases when more weight is given to the outer thrusters. Similarly, when lower thrust weight is given to the outer thrusters, the overall mean thrust usage gets reduced. Due to the better moment effect of outer thrusters mentioned in the torpedo mode operation, modes after 7 use the outer thrusters more and hence have lower overall thrust usage. However, as expected, the average thruster usage is higher than the torpedo mode. Again, for mode 15, configuration C has the

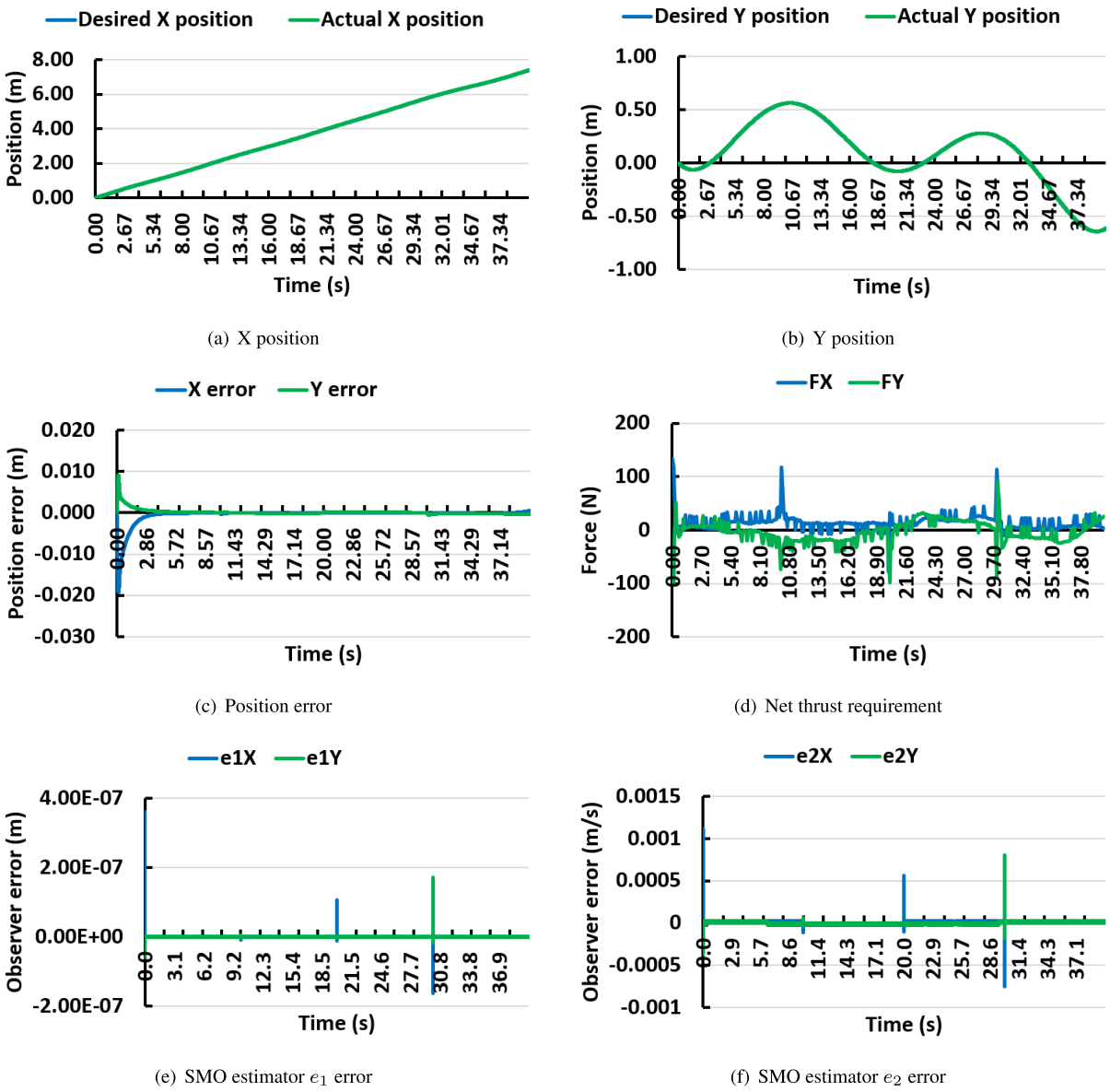

(a) X position (b) Y position

(c) Position error (d) Net thrust requirement

(e) SMO estimator e_1 error (f) SMO estimator e_2 error

FIGURE 13. Variation of different parameters with inspection mode operation.

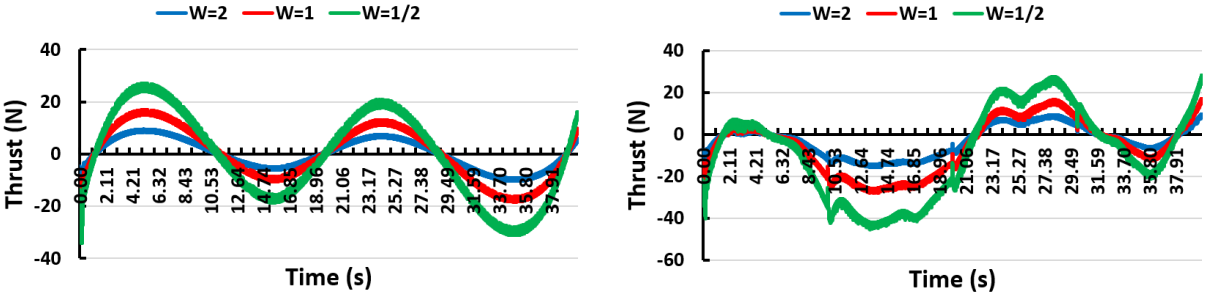

(a) Torpedo operation (b) Inspection operation

FIGURE 14. Variation of the thruster 1 usage with weight modes for torpedo and inspection operations.

lowest mean thrust usage at 5.23 N and B has the highest one at 5.32 N showing the advantage of having individual thrusters located farther to have a better moment effect. When mode 7, the worst mode considered, B peaks at 5.81 N and

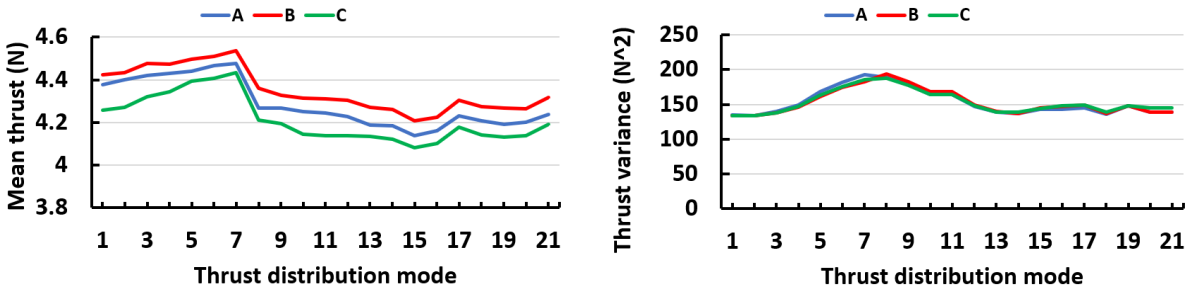

(a) Mean thrust usage (b) Variance in the thrust usage

FIGURE 15. Variation of the thrust parameters with different thrust distribution modes for the torpedo operation.

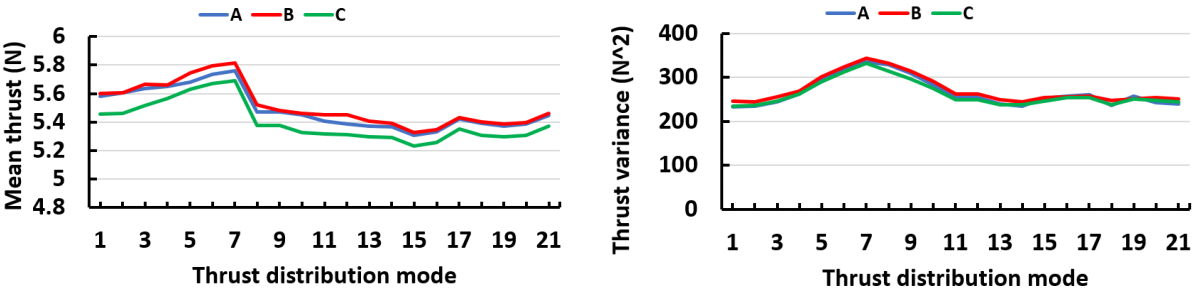

(a) Mean thrust usage (b) Variance in the thrust usage

FIGURE 16. Variation of the thrust parameters with different thrust distribution modes for the inspection operation.

C at 5.69 N. Interestingly, the difference between individual configurations is lesser with the inspection mode compared to the torpedo one. Here also, it is observed that the mean thrust usage is minimal for mode 15, where the denominator value changes from 1 to 2. Similar to the torpedo mode, the second lowest value corresponds to mode 16, where the denominator ranges between 1 and 2.718, which overlaps partly with mode 15. Similar to the torpedo mode, the variation in the thruster usage is calculated with the help of the thrust variance graph shown in Fig. 16 (b). The variance increases until mode 7 and decreases to a steady lower value similar to mode 1. This shows that higher weight given to the outer thrusters causes increased variation in the overall thrust values. In addition, modes from 18 to 21 perform poorly compared to the corresponding modes between 14 and 17, as in the previous case.

VII. CONCLUSION

The dynamics of the 2-dimensional motion of serial split-hull underwater vehicles with general elliptical cross-section hulls are modelled, followed by the design and implementation of an energy-efficient adaptive thrust distribution on the already robust STA-based control system. To obtain general findings and simulate the real-world requirements, different configurations of the proposed split-hull vehicle and operation modes are used. This includes considering three vehicle configurations: A, B and C and torpedo and inspection mode of operations. As part of the state estimation and update, a sliding mode-based SMO is used, which has proved to be one of the best for such a purpose. Stability analyses of the different subsystems are also carried out to ensure the reliability of the overall system, and their findings are used for estimating the parameters for the control and observer systems. It is observed that the vehicle traces the desired trajectory with minimal error due to the robust adaptive STA control, and error values in the observer system are also negligible, indicating its effectiveness.

The adaptive thrust distribution algorithm, which is the main goal of this paper, is evaluated in detail in section V. Instead of choosing a fixed weight for the individual thrusters, as done in the literature, adaptive thruster weight values are used here, which turn out to be reducing the overall average thruster usage and the power consumption during the operation. To do that, the effect of weight on the thruster usage is analysed first by comparing reciprocal weights (W = 2 and 1/2) on the unit weight (W = 1), and it is understood that the higher the weight given to a thruster, the lower will be overall thrust usage and vice versa. This concept is added to the fact that outer thrusters have a higher moment effect on the vehicle C.M, and the adaptive thrust distribution algorithm is implemented. Various feasible thrust distribution modes are used, as shown in Table 3, and with the help of simulations, it is observed that the lower the weight given to outer thrusters, the lower the overall average thrust usage. Furthermore, weight

values between 1 and 1/2 which corresponds to a range in denominator between 1 and 2, give the best results in terms of the mean thrust usage. Comparing the vehicle configuration revealed the advantage of having individual thrusters located farther to have a better moment effect, reducing the overall power consumption. Thus, it is decided to go with configuration C and the mode 15 weight distribution algorithm for the proposed split-hull underwater vehicle.

It is also important to note that the proposed algorithm is applicable to various split-hull underwater vehicles, not limited to the elliptical ones, as the concept is based on the difference in moment vector values for the individual thrusters. As long as the vehicle is over-actuated with multiple serial thrusters and the corresponding dynamic modelling can be generated, this algorithm can be implemented in its control system. Although the trend in reducing the mean thrust usage by giving lower weights to the outer thrusters applies to any split-hull vehicle, the optimal weight mode may depend on the specific hull shape used. To estimate that, a detailed analysis of this algorithm with different hull shapes can be conducted, which leads to extended research work, as mentioned in the future works section. However, as most split-hull underwater vehicles have elliptical/cylindrical hulls [4], [12], the proposed algorithm applies to most such vehicles and this paper is concluded with the same case. More details about the future works are discussed below.

VIII. FUTURE WORKS

The focus of this paper was on improving the average thrust usage by placing more emphasis on the thrust force requirement than on the joint torque. It assumed that the power consumption of the joint sections is uniform between different vehicle configurations and that the joint torque requirement is always within the limit of the servo used. Though it is negligible in practice, extended research can be conducted to find the optimum configuration of the vehicle considering these factors. Also, fixed numbers of hulls and thrusters were considered here, which could be extended by considering various other possible numbers. The entire work focuses on the vehicle's 2D movements, and though it is sufficient for most water body mapping and bathymetry cases, extended work with the 3D scenario is also possible. As a final point, though it is clear from the results that this algorithm can work with different hull shapes as long as the vehicle is over-actuated and the corresponding dynamic modelling can be generated, an extended study can be conducted with different hull shapes to verify it.

APPENDIX

Definition 1: A continuous function $\alpha : \mathbb{R}_{\geq 0} \to \mathbb{R}_{\geq 0}$ is said to belong to class $\mathcal{K}$ if it is strictly increasing and $\alpha(0) = 0$. It is said to be of class $\mathcal{K}_\infty$ if moreover $\alpha(s) \to \infty$ as $s \to \infty$.

Definition 2: A continuous function $\beta : \mathbb{R}_{\geq 0} \times \mathbb{R}_{\geq 0} \to \mathbb{R}_{\geq 0}$ is said to belong to class $\mathcal{KL}$ if, for each fixed s, $\beta(:, s)$ is of class $\mathcal{K}$ and for each fixed r, $\beta(r, :)$ is strictly decreasing and $\beta(r, s) \to 0$ as $s \to \infty$.

Theorem 1: Boundedness theorem by Khalil (Theorem 4.18 in [63]).

Let $D \subset \mathbb{R}^n$ be a domain that contains the origin and $V : [0, \infty) \times D \to \mathbb{R}$ be a continuously differentiable function such that

$$\alpha_1(|x|) \leq V(t, x) \leq \alpha_2(|x|) \tag{110}$$

$$\frac{\partial V}{\partial t} + \frac{\partial V}{\partial x} f(t, x) \leq -W(x), \quad \forall |x| \geq \mu > 0 \tag{111}$$

$\forall\, t > 0$ and $\forall\, x \in D$, where α_1 and α_2 are class $\mathcal{K}$ functions and $W(x)$ is a continuous positive definite function. Take $r > 0$ such that $B_r \subset D$ and suppose that

$$\mu < \alpha_2^{-1}(\alpha_1(r)) \tag{112}$$

Then there exists a class $\mathcal{KL}$ function β and for every initial state $x(t_0)$, satisfying $|x(t_0)| \leq \alpha_2^{-1}(r)$, there is $T \geq 0$ such that the solution of $\dot{x} = f(t, x)$ satisfies

$$|x(t)| \leq \beta(|x(t_0)|, t - t_0), \quad \forall\ t_0 \leq t \leq t_0 + T \tag{113}$$

$$|x(t)| \leq \alpha_1^{-1}(\alpha_2(\mu)), \quad \forall\ t \geq t_0 + T \tag{114}$$

Note that (113) and (114) show the boundedness of the system.

Theorem 2: Uniformly Globally Asymptotically Stable of cascades by Loria and Panteley (Lemma 2.1 in [64]).

Consider the cascaded system:

$$\dot{x}_1 = f_1(t, x_1) + g(t, x)x_2 \tag{115}$$

$$\dot{x}_2 = f_2(t, x_2) \tag{116}$$

where $x_1 \in \mathbb{R}^n$, $x_2 \in \mathbb{R}^m$ and the function f_1 is continuously differentiable in (x_1, x_2). The above cascade system is Uniformly Globally Asymptotically Stable (UGAS) if and only if the systems $\dot{x}_1 = f_1(t, x_1)$ and $\dot{x}_2 = f_2(t, x_2)$ are UGAS and the functions given in (115) and (116) are Uniformly Globally Bounded (UGB).

REFERENCES

[1] T. Prestero, "Verification of a six-degree of freedom simulation model for the REMUS100 AUV," Master's thesis, Massachusetts Inst. Technol., Cambridge, MA, USA, 2001.
[2] N. Goldfarb, J. Wang, S. Bai, and B. Englot, "Toward robust localization and mapping for shallow water ROV inspections," in *Proc. OCEANS MTS/IEEE Washington*, Oct. 2015, pp. 1–7.
[3] L. G. García-Valdovinos, T. Salgado-Jiménez, M. Bandala-Sánchez, L. Nava-Balanzar, R. Hernández-Alvarado, and J. A. Cruz-Ledesma, "Modelling, design and robust control of a remotely operated underwater vehicle," *Int. J. Adv. Robotic Syst.*, vol. 11, no. 1, p. 1, Jan. 2014.
[4] T. Jacobs, "What to expect when you're expecting robots," *J. Petroleum Technol.*, vol. 73, no. 8, pp. 22–29, 2021.
[5] Z. Song, A. Marburg, and D. Manalang, "Resident subsea robotic systems: A review," *Mar. Technol. Soc. J.*, vol. 54, no. 5, pp. 21–31, Sep. 2020.
[6] V. S. Kumar and P. Rajagopal, "Optimising the turning performance of serial split-hull underwater vehicles," *Ocean Eng.*, vol. 261, Oct. 2022, Art. no. 112099.
[7] V. S. Kumar and P. Rajagopal, "Modelling and analysis of turning motion of a subsurface mapping AUV with split-hull design," *J. Mar. Sci. Appl.*, vol. 20, no. 2, pp. 284–301, Jun. 2021.
[8] E. Kelasidi, "Modeling, control energy efficiency underwater snake robots," Ph.D. thesis, Dept. Eng. Cybern., Norwegian Univ. Sci. Technol. (NTNU), Trondheim, Norway, 2015.
[9] B. Tao, H. Sun, and J. Sun, "Dynamic modeling and control of underwater snake robot," in *Proc. IEEE 11th Data Driven Control Learn. Syst. Conf. (DDCLS)*, Aug. 2022, pp. 158–163.

[10] A. M. Kohl, K. Y. Pettersen, E. Kelasidi, and J. T. Gravdahl, "Planar path following of underwater snake robots in the presence of ocean currents," *IEEE Robot. Autom. Lett.*, vol. 1, no. 1, pp. 383–390, Jan. 2016.

[11] I. L. G. Borlaug, J. T. Gravdahl, J. Sverdrup-Thygeson, K. Y. Pettersen, and A. Loria, "Trajectory tracking for underwater swimming manipulators using a super twisting algorithm," *Asian J. Control*, vol. 21, no. 1, pp. 208–223, Jan. 2019.

[12] J. Liu, Y. Tong, and J. Liu, "Review of snake robots in constrained environments," *Robot. Auto. Syst.*, vol. 141, Jul. 2021, Art. no. 103785.

[13] E. Kelasidi, M. Jesmani, K. Pettersen, and J. Gravdahl, "Locomotion efficiency optimization of biologically inspired snake robots," *Appl. Sci.*, vol. 8, no. 1, p. 80, Jan. 2018.

[14] J. Sverdrup-Thygeson, E. Kelasidi, K. Y. Pettersen, and J. T. Gravdahl, "The underwater swimming manipulator—A bioinspired solution for subsea operations," *IEEE J. Ocean. Eng.*, vol. 43, no. 2, pp. 402–417, Apr. 2018.

[15] I. L. G. Borlaug, J. Sverdrup-Thygeson, K. Y. Pettersen, and J. T. Gravdahl, "Combined kinematic and dynamic control of an underwater swimming manipulator," in *Proc. 12th IFAC Conf. Control Appl. Mar. Syst., Robot., Vehicles (CAMS)*, Daejeon, South Korea, vol. 52, no. 21, 2019, pp. 8–13.

[16] S. V. Aalbu, "Subsea inspection and intervention with underwater swimming manipulators," M.S. thesis, Dept. Eng. Cybern., Norwegian Univ. Sci. Technol., Trondheim, Norway, 2018.

[17] G. Antonelli, T. I. Fossen, and D. R. Yoerger, "Modeling and control of underwater robots," in *Springer Handbook Robotics*. Cham, Switzerland: Springer, 2016, pp. 1285–1306.

[18] J. Zhang, Y. Chen, and Y. Gong, "Hybrid dynamic modeling for an underwater rigid-soft snake robot," in *Proc. 12th Int. Conf. CYBER Technol. Autom., Control, Intell. Syst. (CYBER)*, Jul. 2022, pp. 1258–1263.

[19] B. H. Hoffmann, "Path following and collision avoidance for an underwater swimming manipulator," M.S. thesis, Dept. Eng. Cybern., Norwegian Univ. Sci. Technol. (NTNU), Trondheim, Norway, 2018.

[20] M. F. Amundsen, "Control of an underwater swimming manipulator, with compensation for reaction forces and hydrostatic forces," M.S. thesis, Dept. Eng. Cybern., Norwegian Univ. Sci. Technol. (NTNU), Trondheim, Norway, 2017.

[21] K. Zhao, L. Wu, P. Wang, and C. Ren, "Trajectory tracking control of an underwater swimming manipulator with state constraints," in *Proc. 41st Chin. Control Conf. (CCC)*, Jul. 2022, pp. 2260–2265.

[22] R. Ariizumi and F. Matsuno, "Dynamic analysis of three snake robot gaits," *IEEE Trans. Robot.*, vol. 33, no. 5, pp. 1075–1087, Oct. 2017.

[23] T. Ma, L. Wu, Z. Lin, C. Ren, and S. Ma, "Energy optimization of an underwater swimming manipulator with rotary thrusters and rolling joints," in *Proc. 41st Chin. Control Conf. (CCC)*, Jul. 2022, pp. 3717–3722.

[24] S. B. Øvregård, "Control allocation for underwater snake robots using optimization methods," M.S. thesis, Dept. Mar. Technol., Norwegian Univ. Sci. Technol., Trondheim, Norway, 2018.

[25] G. Antonelli and S. Chiaverini, "Singularity-free regulation of underwater vehicle-manipulator systems," in *Proc. Amer. Control Conf.*, vol. 1, Jun. 1998, pp. 399–403.

[26] S. Liu, Y. C. Liu, and N. Wang, "Nonlinear disturbance observer-based backstepping finite-time sliding mode tracking control of underwater vehicles with system uncertainties and external disturbances," *Nonlinear Dyn.*, vol. 88, no. 1, pp. 465–476, Apr. 2017.

[27] O.-E. Fjellstad and T. I. Fossen, "Singularity-free tracking of unmanned underwater vehicles in 6 DOF," in *Proc. 33rd IEEE Conf. Decis. Control*, Dec. 1994, pp. 1128–1133.

[28] D. Zhu and B. Sun, "The bio-inspired model based hybrid sliding-mode tracking control for unmanned underwater vehicles," *Eng. Appl. Artif. Intell.*, vol. 26, no. 10, pp. 2260–2269, Nov. 2013.

[29] T. I. Fossen, "Adaptive macro-micro control of nonlinear underwater robotic systems," in *Proc. 5th Int. Conf. Adv. Robot. Robots Unstructured Environ.*, 1991, pp. 1569–1572.

[30] S. Soylu, B. J. Buckham, and R. P. Podhorodeski, "A chattering-free sliding-mode controller for underwater vehicles with fault-tolerant infinity-norm thrust allocation," *Ocean Eng.*, vol. 35, no. 16, pp. 1647–1659, Nov. 2008.

[31] M. W. Dannigan and G. Russell, "Evaluation and reduction of the dynamic coupling between a manipulator and an underwater vehicle," *IEEE J. Ocean. Eng.*, vol. 23, no. 3, pp. 260–273, Jul. 1998.

[32] R. Cristi, F. A. Papoulias, and A. J. Healey, "Adaptive sliding mode control of autonomous underwater vehicles in the dive plane," *IEEE J. Ocean. Eng.*, vol. 15, no. 3, pp. 152–160, Jul. 1990.

[33] J. Xu, M. Wang, and L. Qiao, "Dynamical sliding mode control for the trajectory tracking of underactuated unmanned underwater vehicles," *Ocean Eng.*, vol. 105, pp. 54–63, Sep. 2015.

[34] R. Cui, X. Zhang, and D. Cui, "Adaptive sliding-mode attitude control for autonomous underwater vehicles with input nonlinearities," *Ocean Eng.*, vol. 123, pp. 45–54, Sep. 2016.

[35] H. Huang, G.-C. Zhang, Y.-M. Li, and J.-Y. Li, "Fuzzy sliding-mode formation control for multiple underactuated autonomous underwater vehicles," in *Proc. Int. Conf. Swarm Intell.* Cham, Switzerland: Springer, 2016, pp. 503–510.

[36] E. Rezapour, K. Y. Pettersen, P. Liljebäck, and J. T. Gravdahl, "Differential geometric modelling and robust path following control of snake robots using sliding mode techniques," in *Proc. IEEE Int. Conf. Robot. Autom. (ICRA)*, May 2014, pp. 4532–4539.

[37] J. Sverdrup-Thygeson, E. Kelasidi, K. Y. Pettersen, and J. T. Gravdahl, "Modeling of underwater swimming manipulators," *IFAC-PapersOnLine*, vol. 49, no. 23, pp. 81–88, 2016.

[38] J. Y. Hung, W. Gao, and J. C. Hung, "Variable structure control: A survey," *IEEE Trans. Ind. Electron.*, vol. 40, no. 1, pp. 2–22, Feb. 1993.

[39] K. D. Young, V. I. Utkin, and U. Ozguner, "A control engineer's guide to sliding mode control," *IEEE Trans. Control Syst. Technol.*, vol. 7, no. 3, pp. 328–342, May 1999.

[40] A. Levant, "Sliding order and sliding accuracy in sliding mode control," *Int. J. Control*, vol. 58, no. 6, pp. 1247–1263, Dec. 1993.

[41] Y. B. Shtessel, J. A. Moreno, F. Plestan, L. M. Fridman, and A. S. Poznyak, "Super-twisting adaptive sliding mode control: A Lyapunov design," in *Proc. 49th IEEE Conf. Decis. Control (CDC)*, Dec. 2010, pp. 5109–5113.

[42] A. Swikir and V. Utkin, "Chattering analysis of conventional and super twisting sliding mode control algorithm," in *Proc. 14th Int. Workshop Variable Struct. Syst. (VSS)*, Jun. 2016, pp. 98–102.

[43] S. Kamal, A. Chalanga, J. A. Moreno, L. Fridman, and B. Bandyopadhyay, "Higher order super-twisting algorithm," in *Proc. 13th Int. Workshop Variable Struct. Syst. (VSS)*, Jun. 2014, pp. 1–5.

[44] K. Kumari, A. Chalanga, and B. Bandyopadhyay, "Implementation of super-twisting control on higher order perturbed integrator system using higher order sliding mode observer," *IFAC-PapersOnLine*, vol. 49, no. 18, pp. 873–878, 2016.

[45] I.-L. G. Borlaug, "Higher-order sliding mode control-stability analysis and application to underwater snake robots," M.S. thesis, Dept. Eng. Cybern., Norwegian Univ. Sci. Technol., Trondheim, Norway, 2017.

[46] A. Chalanga, S. Kamal, L. M. Fridman, B. Bandyopadhyay, and J. A. Moreno, "Implementation of super-twisting control: Super-twisting and higher order sliding-mode observer-based approaches," *IEEE Trans. Ind. Electron.*, vol. 63, no. 6, pp. 3677–3685, Jun. 2016.

[47] E. Kelasidi, K. Y. Pettersen, P. Liljeback, and J. T. Gravdahl, "Locomotion efficiency of underwater snake robots with thrusters," in *Proc. IEEE Int. Symp. Saf., Secur., Rescue Robot. (SSRR)*, Oct. 2016, pp. 174–181.

[48] E. Kelasidi, P. Liljeback, K. Y. Pettersen, and J. T. Gravdahl, "Innovation in underwater robots: Biologically inspired swimming snake robots," *IEEE Robot. Autom. Mag.*, vol. 23, no. 1, pp. 44–62, Mar. 2016.

[49] I.-L.-G. Borlaug, K. Y. Pettersen, and J. T. Gravdahl, "Comparison of two second-order sliding mode control algorithms for an articulated intervention AUV: Theory and experimental results," *Ocean Eng.*, vol. 222, Feb. 2021, Art. no. 108480.

[50] E. Kelasidi, K. Y. Pettersen, J. T. Gravdahl, S. Stromsoyen, and A. J. Sorensen, "Modeling and propulsion methods of underwater snake robots," in *Proc. IEEE Conf. Control Technol. Appl. (CCTA)*, Aug. 2017, pp. 819–826.

[51] J. B. Keller and S. I. Rubinow, "Slender-body theory for slow viscous flow," *J. Fluid Mech.*, vol. 75, no. 4, pp. 705–714, Jun. 1976.

[52] R. G. Cox, "The motion of long slender bodies in a viscous fluid. Part 1. General theory," *J. Fluid Mech.*, vol. 44, no. 4, pp. 791–810, 1970.

[53] J. R. Morison, J. W. Johnson, and S. A. Schaaf, "The force exerted by surface waves on piles," *J. Petroleum Technol.*, vol. 2, no. 5, pp. 149–154, May 1950.

[54] J. N. Newman and J. Grue, *Marine Hydrodynamics*. Cambridge, U.K.: MIT Press, 1977, p. 426.

[55] A. J. Wiens and M. Nahon, "Optimally efficient swimming in hyper-redundant mechanisms: Control, design, and energy recovery," *Bioinspiration Biomimetics*, vol. 7, no. 4, Nov. 2012, Art. no. 046016.

[56] N. Y. Gus'kova, G. V. Makhortykh, and M. G. Shcheglova, "Inertia and drag of elliptic cylinders oscillating in a fluid," *Fluid Dyn.*, vol. 33, no. 1, pp. 91–95, Jan. 1998.

[57] T. I. Fossen and S. I. Sagatun, "Adaptive control of nonlinear underwater robotic systems," in *Proc. IEEE Int. Conf. Robot. Autom.*, vol. 2, Apr. 1991, pp. 1687–1694.
[58] I.-L. G. Borlaug, "Robust control articulated intervention-AUVs using sliding mode control," Ph.D. thesis, Dept. Eng. Cybern., Norwegian Univ. Sci. Technol. (NTNU), Trondheim, Norway, 2020.
[59] J. Yu, L. Liu, L. Wang, M. Tan, and D. Xu, "Turning control of a multilink biomimetic robotic fish," *IEEE Trans. Robot.*, vol. 24, no. 1, pp. 201–206, Feb. 2008.
[60] D. A. Marinho, V. M. Reis, F. B. Alves, J. P. Vilas-Boas, L. Machado, A. J. Silva, and A. I. Rouboa, "Hydrodynamic drag during gliding in swimming," *J. Appl. Biomechanics*, vol. 25, no. 3, pp. 253–257, Aug. 2009.
[61] J. A. Moreno, "Lyapunov function for Levant's second order differentiator," in *Proc. IEEE 51st IEEE Conf. Decis. Control (CDC)*, Dec. 2012, pp. 6448–6453.
[62] A. Polyakov and L. Fridman, "Stability notions and Lyapunov functions for sliding mode control systems," *J. Franklin Inst.*, vol. 351, no. 4, pp. 1831–1865, 2014.
[63] H. K. Khalil, *Nonlinear Systems*, 3rd ed. Upper Saddle River, NJ, USA: Prentice-Hall, 2002.
[64] A. Loría and E. Panteley, "2 Cascaded nonlinear time-varying systems: Analysis and design," in *Advanced Topics in Control Systems Theory*. London, U.K.: Springer-Verlag, 2005, pp. 23–64.
[65] *Version 9.12.0 (R2022A)*, MATLAB, MathWorks, Natick, MA, USA, 2022.

VISHAKH S. KUMAR received the B.Tech. degree (Hons.) in production engineering from the National Institute of Technology, Calicut, India, in 2016. He is currently pursuing the M.S. and Ph.D. degrees with the Centre for Nondestructive Evaluation (CNDE), Mechanical Engineering Department, IIT Madras. His research interests include unconventional underwater vehicles and control system design. He has developed multiple generations of a snake-like split-hull AUV called M-Hull. He is also part of the development team of an AUV designed to operate in the action of waves and a rover designed to drill for sample collection on the martian surface.

PRABHU RAJAGOPAL (Member, IEEE) received the B.Tech. and M.Tech. (D.D.) degrees from IIT Madras and the Ph.D. and Postdoctoral degrees from the Imperial College, London. He has expertise in remote NDE and SHM, focusing on waveguide ultrasonics, robotics, and management of large scale inspection datasets. With over 25 funded projects, 180 technical articles, 23 filings, and a granted IP, he is widely recognized for work on remote asset management in the marine, energy and mobility sectors and a social focus on water, health, and sanitation. His work spans sensing and data management, with the latter leveraging the latest innovations in AI/ML, and blockchain technologies. His work on metamaterials is expanding, with exciting applications for seismic and vibration damping and non-linear ultrasonics. He also helps companies improve sensor performance using simulation, analysis, and analytics.